Title	FABRICATION AND CHARACTERIZATION OF NEW TYPES OF AL2O3 BASED CERAMICS
Author(s)	李, 春亮
Citation	大阪大学, 2000, 博士論文
Version Type	VoR
URL	https://doi.org/10.11501/3169372
rights	
Note	

FABRICATION AND CHARACTERIZATION OF NEW TYPES OF AL$_2$O$_3$ BASED CERAMICS

（新規なアルミナ基セラミックスの作製と特性評価）

2000

CHUNLIANG LI

DEPARTMENT OF MATERIALS CHEMISTRY

FACULTY OF ENGINEERING

OSAKA UNIVERSITY

Preface

The dissertation - prepared in order to fulfil the requirements for the degree of doctor of philosophy in Department of Materials Chemistry, Faculty of Engineering, Osaka University. The present report introduces the recent development on composite materials performed under the keen guidance of Professor Koichi Niihara at Institute of Scientific and Industrial Research during 1997-2000.

The author of the present thesis performed extensive study on a variety of techniques associated with fabricating molecular/cluster level composted ceramics designed for application in electronic industry.

In particular, the main idea followed strictly by the present author, is that of Niihara who first proposed the concept of structural ceramics nanocomposite in 1991, which means to significantly improve the ceramic materials' properties by nano-size dispersion.The long research program established by Prof. Niihara succeeded in development wonderful materials in which the various high mechanical properties of ceramics such as strength, refractoriness and creep resistance could be remarkably improved through this concept.It also resulted in applying the nano-composite concept to functional ceramics, metal and polymer materials and also to the new ceramics materials with multiple functionality – Intermaterials which is attracting much attentions recently.

The above conclusion has been based on extensive and long studies of nano-composites performed by the staff and students under the leadership of Prof. Niihara. All of them investigated various types of nanocomposites – micro/nano hybrid, hard matrix/soft dispersion, soft matrix/hard dispersion and structural/functional ceramics nanocomposites.

Additionally, it has became obvious that the size of dispersion species can present more new functionality for the ceramics which can be extremely important for successful application of ceramics in industry. It was believed that novel properties could be found by reduce the dispersion species size from nano to molecular/cluster level – this kind of composite is so called molecular/cluster composite.

Thus, the present author concentrated on the problems of fabrication and characterization of the molecular/cluster-level composite, through various kind of powder preparation and sintering processes. The study of the effect of the cluster level dispersions on single crystal ceramics was also treated with equal attention by the author.

The major achievement of this study seems to be successful on fabricating the cluster-level composite which exhibits higher mechanical properties than monolith material by using coprecipitation technique and pulse electronic current sintering, while the cluster-level dispersed sapphire shows a complete different plasticity behavior compared with virgin material.

The author hops that the new concepts and findings in this thesis will contribute a large for fabricating new types of cluster composite to develop advanced composite materials in electronics ceramics and other regions.

<div align="right">Chunliang Li</div>

Department of Materials Chemistry
Faculty of Engineering
Osaka University
2-1 Yamada-oka, Suita, Osaka 567-0871
Japan

Contents

Chapter 1

Introduction

1.1 Ceramics

Ceramics materials was defined as the art and science of making and using solid articles which have as their essential component, and are composed in large part of, inorganic nonmetallic materials. Ceramics includes not only materials such as pottery, porcelain, refractories, structural clay products, porcelain enamels, cements, and glass but also non metallic magnetic materials, ferroelectrics, manufactured single crystals, glass-ceramics etc. [1].

Ceramics possess high melting point, excellent chemical stability and low density, which have been expected to be employed as high-temperature structural materials under severe environments. They have been successfully applied to engine components, cutting tools and sealing material [2]. Recently, ceramics are also expanding their application into various functional fields such as electric and magnetic materials.

Ceramics are usually brittle materials as well as the shortcoming of low thermal-shock resistance and machinability, and these features are considerable disadvantage in many applications. The mechanical properties of these ceramics have been improved by the microstructural development throughout the processing improvement. It seems that it is difficult to improve these problems at the same time by above-mentioned structural development technique. Many attempts have been made to improve these problems by incorporating second phase - composites techniques.

1.2 Composites

Ceramics based composites can be classified into two groups in the present moment: microcomposites and nanocomposites.

1.2.1 Microcomposites

In microcomposites, micro-sized second phase such as micro-sized whisker, fiber, platelet and particulate are mainly dispersed at grain boundaries of a matrix (Fig. 1-1a). The improvement in fracture toughness by bridging, pulling-out and crack deflection toughening mechanism is expected in microcomposites cases. However, strength and high temperature properties could sometimes be decreased while toughness has been increased.
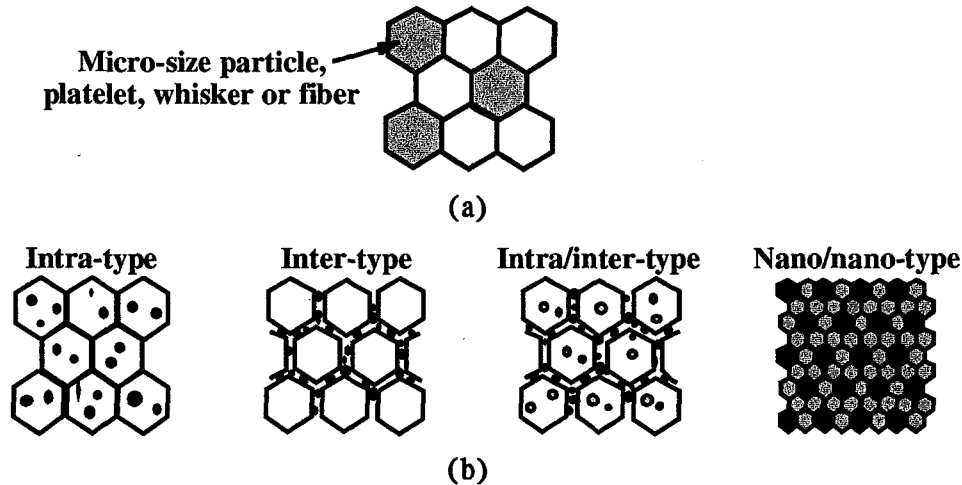
Fig. 1-1 The schematic illustration of typical microcomposites (a) and nanocomposites (b).

1.2.2 Nanocomposite

Nanocomposite materials can be defined as composites of more than one solid phase where at least one of the phases shows dimensions in the nano-meter range [3]. The solid phases can exist either in amorphous, semicrystalline or crystalline states. The concept of structural ceramic nanocomposites was proposed by Niihara in 1991 and it is one of the particulate reinforced ceramic composites, in which nano-sized particulate is dispersed within matrix grain and/or at grain boundaries [4]. Nanocomposites can be further separated into four types: intragranular type, intergranular type, intra/intergranular mixed type, nano/nano type composites as shown in Fig. 1-1b. In the intra- and intergranular nanocomposites, the nano-sized particles are dispersed mainly within the matrix grains or at the grain boundaries of the matrix, respectively. The main aim of these nanocomposite to improve not only the mechanical properties such as hardness, fracture strength and toughness and reliability at room temperature but also high-temperature mechanical properties (i.e., hardness, strength, creep and fatigue fracture resistances). The intergranular nanodispersiods play an important role in the grain boundary structure control of oxide and non-oxide ceramics, which gives the improvement of high-temperature mechanical properties. The nano/nano composites are compared of the dispersiods and matrix grains with the nanometer-size. This kind of composite is proposed to add new functions such as machinability and superplasticity like metals to ceramics.

It was believed that this new materials design concept on nanocomposite could be effective on various ceramic composite systems. Recently, various kinds of ceramic nanocomposite have been studied in ceramic/ceramic [5-9], ceramic/metal [10-13],

intermetallic/ceramic [14] and polymer/ceramic [15] systems. All of these nanocomposites demonstrate significantly improved mechanical properties even at high temperatures.

It was found that the nanocomposite structure would give the in-grain toughening mechanism, which gives the sharp increasing R-curve behavior and is important for the abrasive property improvement of ceramic materials. However, the high toughness will not be obtained through only the nanocomposite structure. Two ways has been attempted to solve this problem - micro/nano hybridization and mutual nanocomposite. On the micro/nano hybridization, the newly developed nanocomposite is reinforced with particulates, whiskers, platelets and long fibers in micro-size. On the mutual nanocomposites, on the other hands, the nano-sized ceramic and metal particulates is dispersed in the micro-sized ceramic and metal grains of the ceramics/metal microcomposites. This mutual nanocomposite structure could be realized even in the ceramic/ceramic composite system.

1.2.3 Recent Study on Nanocomposites

The most important information from recent researches on nanocomposite can be summarized as follows:

- Mechanical properties of the material can be modified by nanocomposite technique, despite what kind of dispersiods has been adopted. It means that fracture strength will be never decreased even by the soft and week second phase dispersions if they are smaller than the critical flaw size of the matrix.

- Other electrical and magnetic properties can be added to the structural ceramics by nanocomposite technique, which quite depend on the properties of dispersions.

- These results give us the chance to fabricate the new structural ceramics with novel functions (i.e., sensing, optical function), while the mechanical properties has been also increased.

- For the case of functional ceramics, both excellent electromagnetic and mechanical properties can be achieved at the same time by nanocomposite technique.

All the above result shows the probability of developing the multi-functional ceramics by nanocomposite technology. These multi-functional ceramics are divided into following groups: hard/soft nanocomposites for the structural ceramics, nanocomposite long fibers with high strength and creep resistance at high temperatures, strong and transparent nano/nano type composites with new optical and magnetic properties, soft/hard

nanocomposites with the improved mechanical and electrical properties for the electronic ceramics, and super-tough and strong micro/nano hybridization composites [16].

1.3 Next Generation's Molecular/Cluster Level Composite

The above conclusion led us to extend the nanocomposite design concept to a completely new type of composite – molecular/cluster-level composite. Molecular/cluster-level composite materials can be defined as composites of more than one solid phase where at least one of the phases shows dimensions in the size of molecular/cluster range. The size of molecular/cluster can be thought as the size of a part of unit cell, which means the size is about or less than one nm. The illustration of cluster-level composites is shown in Fig. 1-2. For the case of Al_2O_3 and Cr_2O_3, the preferred coordination number for aluminum is 6 so that with a valence of 3 there is a bound strength of one-half; this required four Al^{3+} adjacent to each O^{2-}. Therefore, a cluster can be thought as octahedral interstice (AlO_6^{-6}) which means the aluminum ions fills two-thirds of the octahedral site with hexagonal close packing of the oxygen ions.

We can know that the molecular/cluster-sized dispersoids will never decrease the strength of matrix material because they are quite smaller than the critical flaw size of the matrix, according to investigation on the nanocomposites. However, the individual property of the dispersiods (i.e., magnetic and electrical properties) will give the composite which a complete new function which will never be achieved by general method for ceramics material. This kind of material design concept is believed to be useful especially for the electronic ceramics.

Moreover, one can expect that a new generation of ceramic material with novel functionality can be created by making nano/cluster hybridization composites or cluster mutual composite.
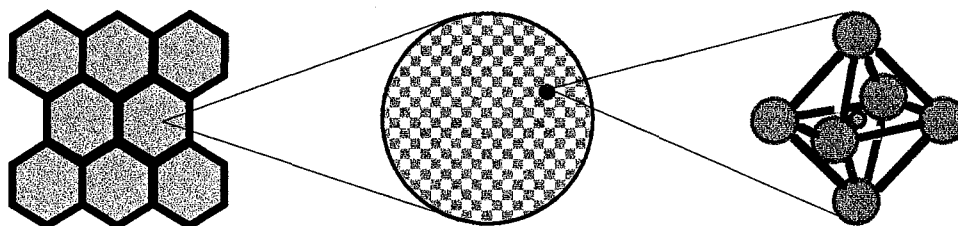

Fig. 1-2 The schematic illustration of typical cluster-level composites.

1.4 Fabrication Methods for New Composites Designed in Molecular/ Cluster Level

Considering the size of the dispersoids, different dispersion methods are required for providing homogeneous and microscopic mixture. The most probable processes to mixture two materials on the level of molecular/cluster size are considered as ion bombardment process, deposition process such as PVD/CVD method for the thin films, and solid-solution process for the bulk materials.

1.4.1 Ion Bombardment Process

The interaction of energetic ions with solids has aroused scientific curiosity ever since the experimental physicist was first provided with beams of charged particles. In 1942, Winger [17] first recognized that energetic neutrons and fission fragments resulting from the nuclear fission process would cause lattice atoms to be displaced from their normal equilibrium positions. He suggested that it might lead to serious technological effects. In 1957, Silsbee [18] pointed out that the transfer of energy and momentum between atoms in a crystalline solid could be strongly influenced by the ordered nature of its lattice. A plenty of theoretical and experimental studies have followed these original discoveries.

Ion bombardment is one of the fields of atomic collision. To perform ion bombardment on the solid surface, one has to ionize the incident atom, accelerate it, and inject into the solid (e.g., impurity doping could be accomplished by implanting impurity ion into the silicon substrate using several hundred keV). The ion trajectory of a single ion of keV energies undergoes a series of energy-loss collisions with both target atoms and electrons. Finally it comes to rest some hundreds of atom layers below the surface. When a number of mono-energetic ions are implanted, the statistical nature of nuclear and electronic energy-loss collisions ensures that not all ions rest precisely of the same depth. The ion-depth profile determined approximately follows a Gaussian form. The peak represents the most probable range of ion penetration. The increase of the dose of incident ions increases the concentration of implanted atoms. Thus, the near-surface composition of the target is modified.

The four basic processes resulted from ion bombardment are implantation, damage, sputtering and atomic mixing, which are schematically illustrated in Fig. 1-3 and 1-4.

Ion Implantation. Ion implantation has been extensively used in past decades and became an essential part of semiconductor device technology. The contraction of ion

implantation led to the important developments in semiconductor materials science. Most of integrated circuits are now fabricated using the above process. Electrical dopants are introduced directly into a semiconductor surface layer by bombarding energetic ions. Ion implantation allows us to control the number and distribution of atoms that are implanted.

Ion implantation can also be used to obtain the wear-resistant coatings, bearing and seals since ion implant can affects the tribological behavior of the hard ceramics. Recently, the above technique is receiving much attention as a method of modifying the surface properties of the metals, polymers, and thin films.
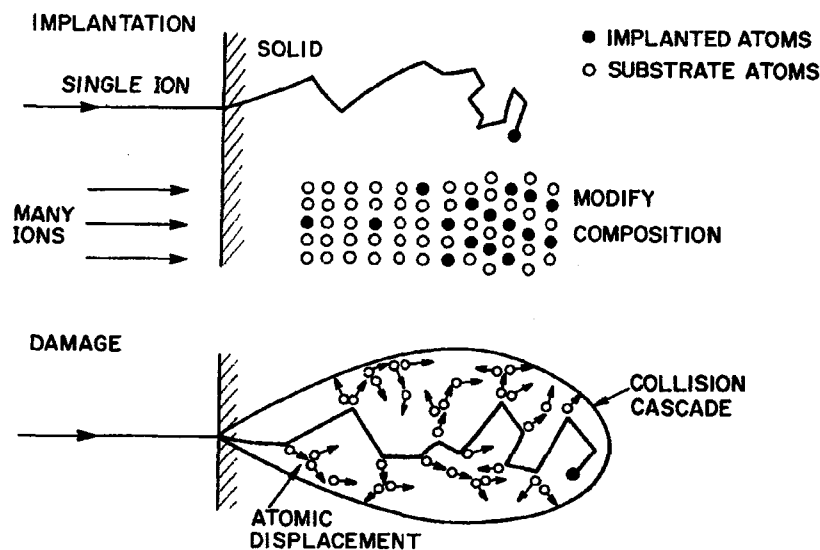

Fig. 1-3 Schematic of the implantation and damage processes using energetic ion beams.
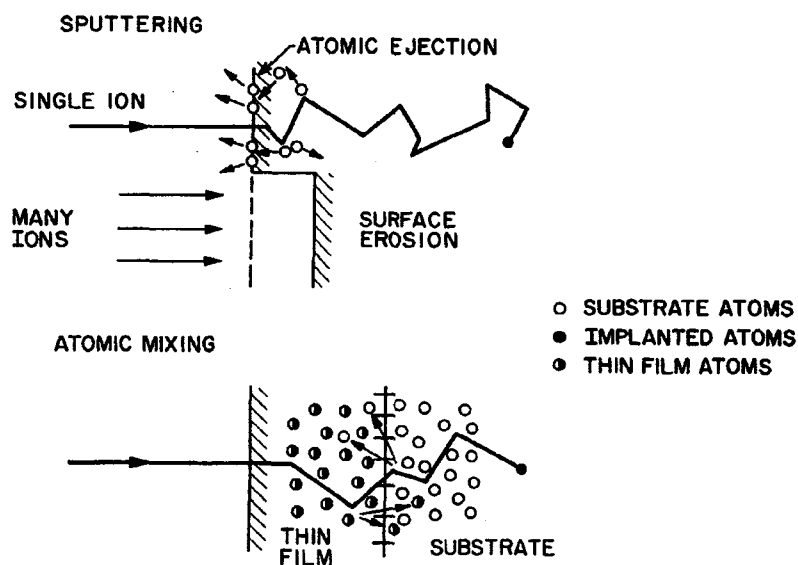

Fig. 1-4 Schematic of the sputtering and atomic mixing processes by energetic ion beam.

6

Radiation Damage. Fig. 1-3 illustrates the radiation damage, whereby lattice atoms are displaced from their regular sites. A single energetic ion can lead to the displacement of many hundreds of lattice atoms within a volume surrounding the ion trajectory.

Ion-beam Sputtering. Within the ion-beam sputtering process, each incident ion can sputter one or more target atoms. Therefore, prolonged irradiation can lead to appreciable surface erosion and to removal of implanted ions. Sputtering often involves collisional processes, energy spikes, electronic effects, and complicated diffusional effects.

Atomic mixing. Ion-beam-induced intermixing can take place across the boundaries of layers of different composition (see Fig. 1-4). The ion mixing method may involve simple collisional mixing or more complicated beam-induced diffusional processes.

Other applications of ion bombardment are also reviewed by Watt and Grime [19] who describe the usage in biology and earth sciences, solid state physics and electronics and detecting ancient bones, teeth, clays, glasses, alloys and gold in archaeology field (for review see ref. 19).

In this study, we has employ this technique to disperse the second phase on cluster level into the single crystal in order to find the possibility of structure control by the molecular/cluster-level dispersiods and their influence on the mechanical properties.

1.4.2 Solid Solutions

When a material crystallizes in the presence of foreign atoms, if building them into the host structure in an ordered way leads to a large lowering of the system's energy, a new crystalline form develops [20]. When solid solution occurs, a change in the cell size with composition in accordance with *Vegard's law* that the lattice-cell dimensions vary linearly with the concentration of solute added. There are two kinds of solid solutions which are shown in Fig. 1-5.

Substitutional Solid Solution. Substitution of one ion for another is common in the formation of ceramic crystals. There are several factors to determine the extent of substitution that can take place in solid solutions.

- Size Factor: The sizes difference of two ions must be less that 15% to form the substitutional solid solution.
- Valency Factor: There are limitations of substitution if the added ion has a valence different from that of the matrix ion.
- Chemical Affinity: The greater the chemical reactivity of the two crystalline materials, the more restricted is solid solubility.
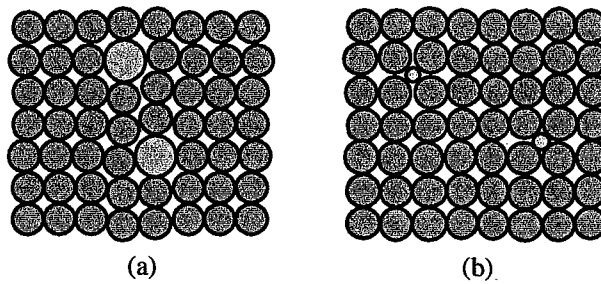
7

Fig. 1-5 Schematic illustration of substitutional (a) and interstitial (b) solid solutions.

- Structure Type: Two materials must have same type of crystal structure for complete solid solubility.

Interstitial Solid Solutions. Added atom can go on interstitial sites in the crystal to form solid solution if they are too small. The ability to form interstitial solid solution depends on the above-mentioned factors for substitutional solid solution except for the structure type – size, valency and chemical affinity.

Solid solution can occurred everywhere for all the materials, disliking ion bombardment and CVD/PVD process which can only produce the modified crystal structure of thin layer. Therefore, solid solution was thought as the only candidate for achieving molecular/cluster level dispersed ceramics.

1.5 Materials in the Present Study

We has selected the single crystal of alumina (sapphire) as the object material to verify the possibility of structure control by the molecular/cluster-level dispersiods which are formed by ion bombardments, while Al_2O_3-Cr_2O_3 solid solution has been adopted to achieve the molecular/cluster level composite.

1.5.1 Alumina Ceramics

Alumina (Al_2O_3) is among the most abundant constituents of the earth's crust, second to silica, which represents 25% of all solid material on the earth's surfaces. Alumina is typically composed of alumina hydrates, such as hydrargillite or gibbsite ($Al_2O_3 \cdot 3H_2O$; $Al(OH)_3$), bauxite ($Al_2O_3 \cdot 2H_2O$; $Al_2O(OH)_4$), and diaspore ($Al_2O_3 \cdot 3H_2O$; $AlO(OH)$). Pure Alumina is a rare mineral (corundum) which is associated with other oxides, such as Fe_2O_3, TiO_2, SiO_2 and Cr_2O_3. These comparatively pure corundums are known as white, yellow, and blue sapphire, and red ruby.
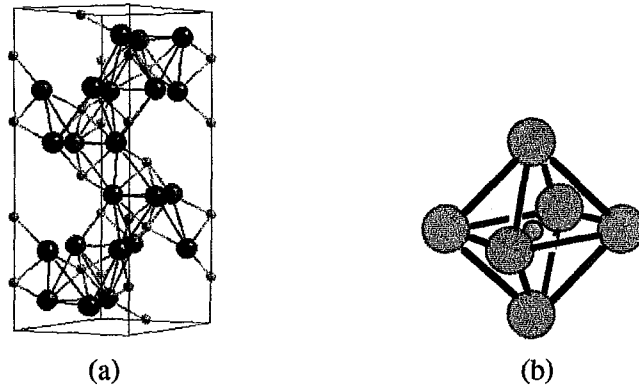
8

Fig. 1-6 The lattice unit of α-alumina (a) and octahedral interstice (b)

Table 1-1 Properties of alumina

Properties	Sintered alumina	Single crystal
Purity (%)	99.5-99.9	100
Density (g/cm^3)	3.9-3.98	3.99
Young's modulus (GPa)	294.2-392.6	411.9
Poisson ratio	0.22	0.25
Strength (MPa)	245.2-539.3	686.5
Knoop hardness (GPa)	22.56	21.57
Thermal expansion coefficient ($10^{-6}/°C$)	7.8-8.1	5.3
Electrical resistance (Ω·cm)	10^{14}	10^{16}

Alumina has various types of crystalline forms such as α-, γ-, δ-, η-, θ-, χ-, and ρ-Al$_2$O$_3$. Only α-alumina has a definitely established stable crystal structure. The unit cell of α-alumina, know as corundum is shown in Fig. 1-6 (a). The oxygen atoms form the closest hexagonal packing inside of which smaller aluminum atoms are enclosed. Each Al atom is surrounded by six O atoms. The average distance between Al and O is 1.92 Å, while 2.495 Å between O atoms. The lattice constant of α-alumina is a=4.758 Å and c=12.991 Å.

α-Al$_2$O$_3$ has a very strong bound, with the highest hardness of the oxide ceramics. The properties of Al$_2$O$_3$ are summarized in Table 1-1. The above mentioned good properties of Al$_2$O$_3$ coupled with ease of fabrication and high density have there made this material desirable for use in a wide field of engineering application compared with other ceramics. It is utilized in engineering applications requiring such properties as strength, abrasive resistance, electrical insulation, optical properties.

9

1.5.2 Al₂O₃-Cr₂O₃ Ceramics

1.5.2 Al_2O_3-Cr_2O_3 Ceramics

Both Al_2O_3 and Cr_2O_3 appear to be a refractory material with high melting point which is appreciated due to its high temperature oxidation resistance [21]. Both Cr_2O_3 and α-Al_2O_3 crystallize in the corundum type of crystal structure and their Al^{3+} and Cr^{3+} ions posses a similar radius (Al^{3+}=0.53 Å, Cr^{3+}=0.62 Å). The above mentioned coincidence of lattices and ionic radii makes it possible to obtain the perfect, continuous solid solution of the discussed materials at temperatures as high as 900°C [22].

Because the size of Cr^{3+} is bigger than Al^{3+}, the Cr_2O_3 possess a bigger lattice constant (a=4.9607 Å and c=13.599 Å) compared with Al_2O_3 crystal. Therefore, when the AlO_6^{-6} cluster is replaced with CrO_6^{-6} cluster, internal stress will be created between CrO_6^{-6} cluster and the surrounding AlO_6^{-6} clusters, as shown in Fig. 1-7. This allows us to control the alumina crystal structure on the cluster level by dispersing the CrO_6^{-6} cluster. It was expected that the stress created by solid solution will have a bigger influence on the mechanical properties of alumina ceramics.
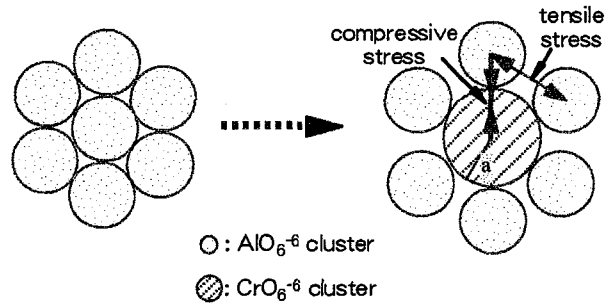
Fig. 1-7 The illustration of AlO_6^{-6} cluster replaced with CrO_6^{-6} cluster.

1.6 Nano-indentation

The idea of depth-sensing indentation measurements which allow estimation of Young's modulus of materials has already been realized in past decade [23]. The first reports on the nano-indentation techniques appeared ten years ago [24-26]. In particular, the report by Pethica *et al.* [27] has been widely recognized and had a great impact on the creation of a new and expanding area - surface deformation of solids. Some recent studies include observations of the propagation of indentation cracks in ceramics, together with the ability to measure the indentation load versus depth curves [28,29], application of the nano-

indentation method for measuring the residual stress [30] and the adhesion [31] in thin surface coating, determination of Young's modulus and the hardness of high-temperature superconductors [32], study of the electrical resistance of metallic contacts on semiconductors during indentation involving phase transformation [33], observation of the structural changes in nano-indented sapphire by means of high resolution electron microscopy [34], and study of the deformation and the fracture of ion-implanted ceramics [35,36].

1.6.1 Indentation System

The numerous reports on ultra-micro or nano indentation systems have been appeared over the last two decades. The new ultra-micro indentation system like UMIS 2000 (CSIRO, Australia) [37] allow additionally to select a number of loading and unloading steps which enable us to obtain the desired accuracy of the measurement.

The UMIS 2000 system is schematically illustrated in Fig. 1-8 . The resolution of depth and force of UMIS 2000 are 0.2 nm and 5 mN, respectively. The maximum loads and displacement ranges are 5 N and 50 µm, but they can also be selected according to particularly requirements. The system operates automatically after initial setup and collects force displacement data at pre-selected sites or arrays of points across the specimen. It can also be operated under displacement or force control with the rate of loading and unloading variable as well as options for rapid loading.
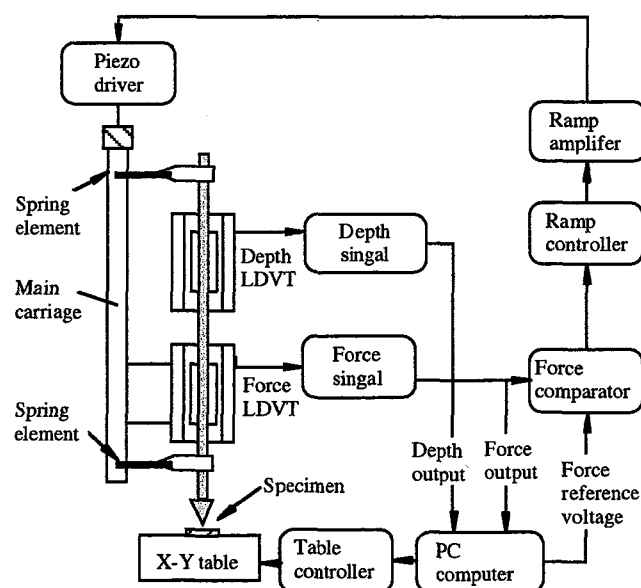

Fig. 1-8 Schematic diagram of the Ultra Micro Indentation System (UMIS-2000)

Vibration, noise and thermal changes can lead to reduction of sensitivity and drift in the data. To minimize these influences, the system is put in an enclosed environment. Force and displacement are independently measured to remove the problem of drift and hysteresis of the displacement or force generating system. The UMIS system also has additional options of a high-resolution optical microscope and an acoustic emission attachment. The latter enables us to register the onset of cracking in brittle films or materials to be detected.

1.6.2 Indenters

Indentation with a steel ball, introduced by Brinel [38] early this century, provides a means of quantifying the different qualities of iron and steel. Because stress strain curves can easily be obtained in unaxial tension and compression, the use of spherical indentation has been largely ignored. However, the Brinel test is limited to use because of the dependence of hardness number on test condition, the larger size of indentation, deformation of the steel ball, soft materials. The Vickers, Knoop and Rockwell tests, which use small diamond pyramids or cones, were introduced to avoid these problems and become industry standards. The two former tests have also been used at very low loads to measure the hardness of thin films or small volumes of materials. More recently, instrumented micro mechanical probe system using Berkovich indenters has been developed to enable the hardness and modulus of localize volumes or thin films to be investigated.

Two kinds of indenters: spherical and pointed (Berkovich) are used in UMIS 2000 system. For the spherical indenter, the contact zone is deformed elastically, while a transition from elastic to plastic deformations then occurs at larger loads. The stress is axisymmetrical, with no preferred direction, so that the orientation of the indenter does not play a role in the determination of properties of crystals and anisotropic materials. Moreover, there is less danger of cracks being too readily formed. On the contract, the usage of Berkovich indenter is rationalized of its sharper tip. Stresses beneath the tip of these indenters are very high. The distribution of stress in a homogeneous material is similar for any depth of indenter penetration.

1.6.3 Measurements

Two measurement cycles are provided in the ultra-micro indentation system UMIS 2000 [37]: a continuous load-unload cycle which produces a record of penetration depth as the indenter is incrementally loaded and unloaded; and a load-partial-unload cycle in which the loading is incremental to a set value followed by an unloading to an intermediate value
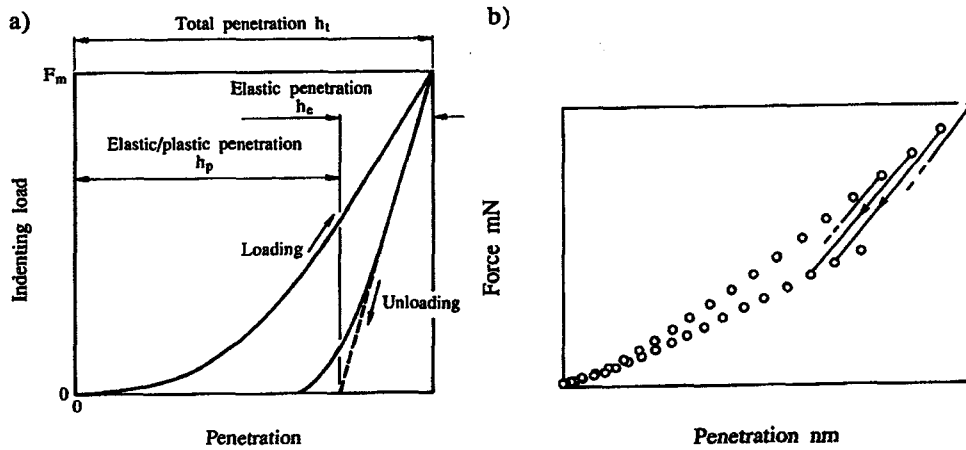
Fig. 1-9 Continuous load-unload (a) and load partial-unload data acquisition cycles (b) measured by UMIS 2000 system.

(this sequence is repeated until maximum load is reached). These two measurement cycles are illustrated in Fig. 1-9.

The data obtained from depth-sensing indentation systems are load, displacement and time. They are generally presented as a diagram of load versus displacement such as shown in Fig. 1-9a. In principle, the load-displacement curve contains complete information about mechanical behavior of the material [38]. Thus, several material parameters might be derived from the curve. However, the data interpretation is complex, since the indentation with a sharp indenter introduces inevitably plastic deformation and no analytical model exists for such a case.

The elastic-plastic indentation contact has been variously modeled by numerous researchers based on the solutions of elastic contact problems with axisymmetric rigid punches or isotropic rigid half-spaces. The above mentioned oversimplified approaches together with their direct applications to the depth-sensing experiments by Doerner and Nix [39] or Oliver and Pharr [40] have been already critically reviewed by Nowak [41].

It is worth noticing that the qualitative analyses of the indentation curves combined with the supporting experimental techniques have been successfully used to clarify novel phenomena occurring during the nano-indentation process. Consequently, Page et al. [42] provided us with an excellent comparative discussion of the nano-indentation experiments on sapphire, silicon and SiC crystals supported by an examination of the indentation deformed region with the help of transmission and scanning electron microscopy. They clarified the origin of the discontinuities observed in load-displacement curves, which appeared when the (0001) plane of α-Al_2O_3 crystal was deformed using a triangular indenter,

13

while Weppelmann *et. al.* [43,44] discovered that the characteristic pop-outs appearing in the unloading curves of silicon are caused by the pressure-induced phase transformation. The pop-ins appearing in the loading curves for higher-load indented sapphire has been clarified by Niihara *et. al.* [45].

1.7 Objectives of This Research

The main objective of the present thesis is to develop a ceramic material with microstructure controlled by cluster-sized dispersiods – molecular/cluster-level composite. Attentions were focused on the mixing process, powder, sintering method, temperature, volume and other relevant conditions for the fabrication and characterization cluster-level composites. The effect of molecular/cluster-sized dispersiods on the crystal microstructure and mechanical properties prepared by ion bombardment have also been evaluated by nano-indentation method. General powder metallurgical method has been adopted to prepare Al_2O_3-Cr_2O_3 nanocomposites with inclined interface on the grain boundary. Coprecipitation method was selected to obtain the homogeneously dispersed Al_2O_3-Cr_2O_3 mixture on the cluster level. Further, the cluster-level composite was achieved by using the new pulse electric current sintering process (PECS). This cluster-level controlled material shows an advanced mechanical properties than normally produced monolithic material. Finally, at the end of thesis, some conclusion has been drawn and some suggestions have been point out for future research works and to utilize these materials on electrical applications. This thesis consists of six chapters depending on the dispersion process and they are briefly described as follows.

In chapter 1, the history of microcomposites and nanocomposites has been reviewed, and the objective and contents of this study are described.

In chapter 2, in order to confirm the influence of the cluster-sized dispersiods, ion implantation has been selected to mix the Ni^{2+} and Au^{2+} ions with sapphire on the cluster level. The mechanical properties of modified samples have been investigated under nano-indentation measurement.

In chapter 3, the Al_2O_3-Cr_2O_3 solid solutions were fabricated by using the conventional powder metallurgical process from commercially available powders. The effects of the amount of Cr_2O_3 additions and the sintering condition on the microstructure and mechanical properties was evaluated.

In chapter 4, a novel coprecipitation process has been attempted to obtain the homogeneously mixed Al_2O_3-Cr_2O_3 powder. The influence on powder microstructure of the conditions of coprecipitation and calcination process are focused by the present author.

In chapter 5, the homogeneous Al_2O_3-Cr_2O_3 mixture has been sintered by using the PECS method. The microstructure and mechanical properties have also been investigated, in accordance with developing the cluster-level composite.

Finally, in chapter 6, summary of this thesis has been drawn. Some visions in fabricating and applying molecular/cluster ceramic composites have been suggested for further researches in the next century.

Reference

1   W.D. Kingery, H.K. Bowen and D.R. Uhlmann, in Introduction to Ceramics, John Wiley & Sons Inc., 1976

2   Y. Moriyoshi, T. Sasamoto, K. Uematsu and Y. Ikuma, Fundamental Science of Ceramics, Uchida Rokakuho Publishing Co., Ltd., Tokyo, 1990, pp. 113-116

3   R. Roy, R.A. Roy and D.M. Roy, Mater. Lett., 4, 323-328 (1986)

4   K. Niihara, J. Ceram. Soc. Jpn., 99, 974-982 (1991)

5   K. Niihara, A. Nakahara, T. Uchiyama and T. Hirano, in Fracture Mechanics of Ceramics, 7, Eds. by R.C. Bradt, A.G. Evans, D.P.H. Hasselman and F.F. Lange, Plenum Press, 1986, pp. 103-116

6   A. Nakahara and K. Niihara, in Fracture Mechanics of Ceramics, 7, Eds. by M. Sasaki, R.C. Bradt, D.P.H. Hasselman and D. Munz, Plenum Press, 1992, pp. 165-178

7   T. Ohji, A. Nakahira, T. Hirano and K. Niihara, J. Am. Ceram. Soc., 77, 3259-3262 (1994)

8   E. Yasuda, Q.Bao and K. Niihara, J. Ceram. Soc. Jpn., 100, 514-519 (1992)

9   G. Sasaki, H. Nakase, K. Suganuma, T. Fujita and K. Niihara, J. Ceram. Soc. Jpn., 100, 536-540 (1992)

10 T. Sekino, A. Nakahira, M. Nawa and K. Niihara, J. Jpn. Soc. Powder Powder Metall., 38, 326-330 (1991)

11 M. Nawa, T. Sekino and K. Niihara, J. Mater. Sci., 29, 3185-3192 (1995)

12 T. Sekino and K. Niihara, Nanostruct. Mater., 6, 663-666 (1995)

13 M. Nawa, K. Yamazaki, T. Sekino and K. Niihara, J. Mater. Sci., 31, 2848-2858

14 A. Nakahira, H. Tamada and K. Niihara, J. Jpn. Powder Powder Metall., 41, 514-517 (1994)

15 K. Niihara, Y.-H. Choa, M. Hussain, Y. Hamahashi, H. Kawahara, Y. Okamato and H. Nishida, Materials Integration, 12 (5), 47-53 (1999)

16 K. Niihara, T. Kusunose, S. Kohsaki, T. Sekino and Y.-H. Chao, Key Engineering Materials, 161-163, 527-534 (1999)

17 E. P. Wigner, J. Appl. Phys. 17, 857, 1946

18 R. H. Sildbee, J. Appl. Phys. 28, 1246, 1957

19 F. Watt and G. W. Grime, in: "Principles & Applications of High-energy Ion microbeams", Adam Hilger, Bristol, 1987

20 W. D. Kingery, H. K. Bowen and D. R. Uhlmann, in: "Introduction to Ceramics", John Wiley & Sons, Inc., 1976

21 W. H. Giltzen, in: "Alumina as a ceramic Material", American Ceramic Society, Columbus, OH, 1970

22 E. N. Bunting, J. Res. Nat. Bur. Stand. , 6, 947-949 (1931)

23 W.J. Cousins, R.W. Armstrong and W.H. Robinson, J. Mater. Sci. 10, 1655-1661 (1985)

24 D. Newey, M.A. Wilkins and H.M. Pollock, J. Phys. E. Sci. Instrum. 15, 1655-1664 (1982)

25 J.B. Pethica, R. Hutchings and W.C. Oliver, Philos. Mag. A48 (1983) 593

26 P.E. Wierenga and A.J.J. Franken, J. Appl. Phys. 55 , 4244-4247(1984)44

27 R. F. Cook and G. M. Pharr, J. Am. Ceram. Soc. 73, 787 (1990)

28 R. Tandon, D. J. Green, and R. F. Cook, J. Am. Ceram. Soc. 73, 2619 (1990)

29 W. R. LaFontaine, C. A. Paszkiet, M. A. Korhonen, and Che-Yu Li, J. Mater. Res. 6, 2084 (1991)

30 D. Stone, W. R. LaFontaine, P. Alexophoulos, T-W. Wu, and C-Y. Li, J. Mater. Res. 3, 141 (1988)

31 B. N. Lucas, W. C. Oliver, R. K. Williams, J. Brynestad, and M. E. O'Hern, J. Mater. Res. 6, 2519 (1991)

32 G. M. Pharr, W. C. Oliver, R. F. Cook, P. D. Kirchner, M. C. Kroll, T. R. Dinger, and D. R. Clarke, J. Mater. Res. 7, 961 (1992)

33 T.F. Page, W.C. Oliver and C.J. McHargue, J. Mater. Res. 7, 450 (1992)

34 M. E. O'Hern, C. J. McHargue, C. W. White, and G. C. Farlow, Nucl. Instrum. Methods B46, 171 (1990)

35 R. Nowak, K. Ueno and K. Kinoshita, in: "Fracture Mechanics of Ceramics", edited by R. C. Bradt, D. P. H. Hasselman, D. Mung, M. Sakai, and V. Ya. Shevchenko (Plenum Press, New York, 1992), Vol. 10, pp. 155-174

36 "UMIS 2000 Ultra Micro-Indentation System Operating Manual", Division of Applied Physics (CSIRO, Australia, 1995), pp. 15-36

37 J. A. Brinell, Congress Int. des Methods d'Essai des Mat. de Construction, Paris 2, 83 (1901)

38 E. Söderlund and D.J. Rowcliffe, J. Hard Mater. 5 (1994) 149

39 M.F. Doerner and W.D. Nix, J. Mater. Res. 1 (1986) 601

40 W.C. Oliver and G.M. Pharr, J. Mater. Res. 7 (1992) 1564

41 R. Nowak and M. Sakai, J. Mater. Res. 8, 1068-1078 (1993)

42 E.R. Weppelmann, J.S. Field and M.V. Swain, J. Mater. Res. 8 (1993) 830-840

43 E.R. Weppelmann, J.S. Field and M.V. Swain, J. Mater. Sci. 30 (1995) 2455-2462

44 R. Nowak, T. Sekino and K. Niihara, Phil. Mag. A74, 171-194 (1996)

Chapter 2

Comparison of Implantation of Ni^{2+} and Au^{2+} Ions
on the Indentation Response of Sapphire

The mechanical behavior of sapphire modified by bombardment with energetic Ni^{2+} and Au^{2+} ions (E=3 MeV, fluence of 2×10^{16} cm^{-2}) was examined by means of ultra micro-indentation in the (1010) plane of virgin and ion-treated crystal. The variation of hardness and Young's modulus with depth of penetration of indenters with pointed or spherical tipped was determined. The spherical tip indenter revealed a dramatic difference in the response of the virgin (overload driven 'pop-in' of the plastic deformation) and implanted (smooth transition from the elastic to plastic response) sapphire. Microscopic observations of the indented surface revealed slip/twin traces close to the impressions in the unimplanted material, but not in ion-modified crystals. The results were rationalized in terms of the ease of plastic deformation or twinning as influenced by irradiation. This results point out that the molecular-level dispersed particles by ion implantation can modified the essential mechanical properties of the ceramics materials which can inhibit the occurrence of destruction of ceramics materials.

2.1. Introduction

2.1.1. Investigations of Sapphire Modified by Ion-Beam Treatment

Alumina has been considered for a long-time as a strong candidate for the first-wall insulator in fusion nuclear reactors. Extensive investigation of Al_2O_3 irradiated with fast and epithermal neutrons started in the late 1950s [1], and the first review of the subject appeared in 1968 [2]. The early research with ion-bombarded alumina was performed to simulate, in a controlled manner, the conditions of the radiation (mainly with neutrons) prevailing in a reactor core [3].

The pioneering work by Arnold et al. [4] addressed variations of optical absorption, residual stress and volume expansion of sapphire being exposed to irradiation with H^+, He^+, D^+, N^+, O^+, Ar^+ and Ar^{2+}species (E=40~500 keV), in terms of atomic displacement, ionization and structural properties. Furthermore, Krefft and EerNisse [5] clarified the origin of anisotropic expansion of both single and polycrystalline aluminum oxides after bombardment with energetic light ions (E=100~500 keV).

Following the early studies of the disorder produced by ion-bombardment in the

structure of Al_2O_3 crystals [4-6], McHargue et al. [7,8] and Naramoto et al. [9,10] reported a considerable increase of hardness and fracture toughness, measured for the basal plane of sapphire after implantation with Cr (E=300 keV, fluence=10^{16}~10^{17} cm^{-2}), Zr or Ti (E=150 keV, fluence=10^{16} cm^{-2}) ions. They investigated the observed effect to a substantial damage of the lattice of sapphire. The authors assessed the damage of the crystal structure using Rutherford backscattering (RBS) [7], RBS channeling [8-10], transmission and scanning electron microscopy (TEM and SEM) and convergent-beam electron diffraction techniques [8], while the reference [9,10] investigated the location of the implanted species from the results of electron paramagnetic resonance (EPR).

Furthermore, Farlow et al. [11,12] who investigated sapphire implanted with Fe, Mn, Ni, Ti, Cr and Ge energetic ions observed that a considerable number of defects that were created in the modified region of the crystal recombined during the implantation process, forming a less defective crystalline near-surface region in Al_2O_3. They found that the hardness variations correlate with the degree of residual lattice damage.

Thorough investigations of alumina crystals bombarded with Ar^{2+}, N^+ and Ni^+ ions of an energy ranging from 300 to 800 keV (fluence 10^{14} to 10^{17} cm^{-2}) were undertaken by Hioki and coworkers [13-16], who clarified the variations of hardness, fracture toughness and flexural strength with implantation dose. They showed with detailed studies the dependence of the mechanical behavior of the crystals on the residual compressive stress generated in the near-surface region by ion bombardment [13, 14], and discussed the effect of amorphization, of sapphire when bombarded with a high dose, on its mechanical characteristics [14-16]. Interestingly, they found that the amorphized surface-layer, which appears to be considerably softer than sapphire, remains under high compressive stresses [16].

The amorphization of Al_2O_3 crystals modified by Cr^+, Ti^+, Y^+ and Zr^+ ions (E=300 keV, fluence=10^{16} to 7×10^{17} cm^{-2}) and their surface stress were studied by Burnett and Page [17,18], who also discussed the indentation deformation and fracture in the vicinity of Vickers and Knoop-type impressions on the plane of ion-treated sapphire. In a further study, McHargue et al. [19, 20] clarified the implantation conditions (dose, energy and temperature) necessary to amorphize the surface of alumina crystals, the dependence of the surface stress on implantation conditions [20] and phase transformation (amorphous to crystalline-sapphire) during annealing of self-implanted sapphire [21]. Romana et al. [22] performed an extensive X-ray diffraction investigation of the structure of alumina amorphized after bombardment with niobium ions (E=150 keV, fluence=5×10^{15}~5×10^{17} cm^{-2}). Finally, a definitive study on the short-range order and changes of near-neighbor bond

length in sapphire implanted with Fe ions was made by McHargue et al. [23, 24] using a number of advanced techniques for surface characterization, e.g. conversion electron Mössbauer spectroscopy, X-ray photoemission spectroscopy, extended X-ray absorption fine structure, X-ray absorption near-edge structure, and selected area electron diffraction.

Ever since high-energy ion beams became available in many laboratories, numerous studies have dealt with sapphire bombarded with ions of the energy in MeV range. The first report of this kind was presented by McHargue et al. [25], who found a residual stress in Al_2O_3 crystal modified with Fe ions (E=1, 2, and 3 MeV, fluence=$1{\sim}4{\times}10^{17}$ cm^{-2}) as high as 1.1 GPa. This was followed by a study of radiation effects separate from those induced by implanted impurities (E=1.5, 2 MeV, fluence=$5{\times}10^{16}{\sim}8{\times}10^{16}$ Fe^+ cm^{-2}) by Allen and Pedraza [26], and of absorption and luminescence in sapphire implanted with iron (E=3.8 MeV, fluence=$2{\times}10^{16}$ cm^{-2}) and copper (E=750~1500 keV, fluence=$10^{15}{\sim}10^{18}$ cm^{-2}) [27] while Nowak et al. [28] investigated fracture of sapphire implanted in the MeV energy range.

Despite all the above work, there has been very little effort to determine the variations of the onset of yield of ion-beam modified sapphire. Since ceramics treated with highly energetic ions posses a thicker modified surface layer which effectively reduces their brittleness [28], the present report concentrates on the deformation of sapphire bombarded in the MeV energy range.

2.1.2. Surface Deformation of Ion-beam Modified Sapphire

Since the volume available for experimental investigations in ion-beam modified materials is very small, the indentation technique appeared naturally as a method for investigating the mechanical properties of these solids. Consequently, a number of studies reported low-load Vickers or Knoop hardness as the essential parameter characterizing the modified surfaces [7-11, 15-20, 29]. However, a conventional hardness test is frequently insufficient to estimate the mechanical properties of the implanted region because of its limited accuracy. Moreover, the results of the measurements are strongly affected by the presence of the virgin material located directly under the ion-modified surface zone, even for low-load indentation (the substrate effect).

Ever since the availability of nano-indentation testers (see pioneering studies by Newey et al. [30] and Pethica et al. [30]), they have been applied to ion-implanted metals [31], and the first depth-sensing indentation on sapphire was reported by O'Hern et al. [32] for the crystal implanted with Cr ions (E=150-180 keV, fluence=10^{15}-10^{17} cm^{-2}). They registered the characteristic pop-in in the loading-cycle of virgin sapphire indented with a load as low as 2

mN (undetected in the case of ion-implanted crystal) -the effect clarified by Page et al. [33] as caused by the generation of the first dislocations under the indenter. Similar pop-ins were observed in the case of indented alumina by Page et al. [33], Nowak and Sakai [34], as well as by Ensinger and Nowak [35] for the virgin and ion-modified plane of sapphire (E=80 keV, fluence=10^{15}-10^{17} Ta^+ cm^{-2}) deformed with higher loads (2 N). The above indentation experiments were made with sharp conventional indenters (Knoop, Vickers) [7-11, 15, 17-20, 25, 28, 34] or Berkovich-type indenters [32, 33].

Since it has been recently recognized that nano-indentation experiments with spherical tips are able to quantify the localized stress-strain behavior of bulk and thin film ceramic materials (for a review see Swain [36]), the present study deals with the deformation of ion-beam modified sapphire induced by a spherical indenter. It made possible to compare the results with those by Nowak et al. [37] who clarified the origin of the pop-ins observed for higher indentation loads.

The present research addresses the deformation of the (1010) plane of sapphire, in contrast to previous studies devoted mostly to the deformation of the basal plane (a few reports relate to the {1210} and {1012} planes). The indentation results were supported by microscopic observations which allowed us to discuss the differences in deformation of the (1010) plane of sapphire modified by bombardment with highly energetic (3 MeV) Ni^{2+} and Au^{2+} ions.

Another important purpose in this study is to confirm the possibility of stuctrure control on the level of molecular/cluster size, the influence on mechanical properties of the cluster-size dispersiods, which is introduced by bombarding the Ni^{2+} and Au^{2+} ions into sapphire.

2. Experimental

The sapphire crystals (size of approximately 8×10×1 mm) used in the present study were obtained by Kyocera using the edge-defined, film-fed growth method. A special sequence of thermal treatment and polishing was used in order to produce a perfectly flat crystal surface, free from defects and residual stresses [34]. The orientation of the crystal surfaces was confirmed by the Laue X-ray diffraction technique, while the degree of perfection of the near-surface region has been examined using the reflection high-energy electron diffraction patterns. The latter confirmed that the stresses usually induced by the polishing process were not present in the vicinity of the surface.

21

The prismatic plane of sapphire was selected for the present investigation. It was bombarded with 3 MeV ions of Ni^{2+} and Au^{2+} to a fluence of 2×10^{16} cm^{-2}. The incident beam was inclined 7° to the direction in order to avoid a channeling effect.

The range of implanted species was estimated using TRIM-code calculations. Consequently, the peaks of the depth profile of implanted nickel and gold ions were located at 1140 and 680 nm, respectively. The deposited energy per ion for gold ions was one order higher than for nickel.

Ultra micro-indentation was performed using indenters with pointed (Berkovich-type) or spherical (nominally 2 micron radius) tips. The variations of the indentation load (indentation hysteresis loops), hardness and Young's modulus with the depth of penetration were determined for maximum indentation loads ranging from 50 to 500 mN. For reference the Berkovich indenter was loaded up to 100 mN. The experiments with the spherical tipped indenter were made in two modes, the so-called `continuous test' and `the load partial-unload' pioneered by Field and Swain [38]. The latter enabled us to accomplish a near continuous assessment of the contact pressure and elastic modulus versus depth of penetration and of the indentation stress (contact pressure) versus indentation strain (contact radius/indenter radius).

Load partial-unload tests were performed over a range of maximum loads (P_{max}=50, 100, 200, 300, 400 and 500 mN) in an attempt to critically determine the onset from elastic to plastic response of the implanted regions. Analysis of the load partial-unload tests requires knowledge of the effective radius of the indenter as a function of contact depth of penetration because of the inability to polish a perfectly spherical surface on the highly anisotropic diamond indenters. As discussed in the reference paper [36] the effective radius of the indenter versus contact depth was calibrated from indentations on a fused silica sample of known properties.

Several precautions were undertaken in order to guarantee the high accuracy of indentation experiments, e.g. a very low loading rate (0.25 mN s^{-1}) was used in order to allow the material to relax generated stresses and the temperature inside the environmental enclosure of the ultra-micro indentation system varied by less than 0.1°C during the test. The residual impressions have been examined using atomic force microscopy (AFM) which allowed us to register the profile of the deformed surface.

2.3. Results

2.3.1. Continuous Indentation with Triangular and Spherical Indenters

Typical load-displacement curves registered for a triangular indenter penetrating into the plane of sapphire are shown in Fig. 2-1. The results indicate only minor differences in maximum penetration depth measured for virgin and ion-modified surfaces of the crystal, while the hysteresis-loops remain smooth, similar to those reported for the prismatic plane of sapphire by Nowak & Sakai [34]. Closer inspection of the data shows us that the hardness is maximum for the Ni-implanted and minimum for the Au-implanted sapphire which was also tested with low load Vickers and Knoop indentations [28].

In contrast to the results obtained for Berkovich indentation, the load-displacement curves for indentations with a spherical indenter on adjacent regions reveal a strong difference in mechanical characteristics of the virgin, gold implanted and nickel implanted sapphire (Fig. 2-2). Virgin sapphire exhibits an elastic response in the low-load interval, while a distinct pop-in event registered for higher loads characterizes the onset of non-linear behavior.

For the implanted crystals, the elastic regime is much more limited (Fig. 2-2). For loads beyond the elastic limit of the virgin material, the ranking of the penetration is the same as for the Berkovich indenter. It should be emphasized, however, that in the case of the spherical indenter the observed differences are well expressed (Fig. 2-2). The critical load for the pop-in event varies over a range of loads, as previously observed by Nowak et al.
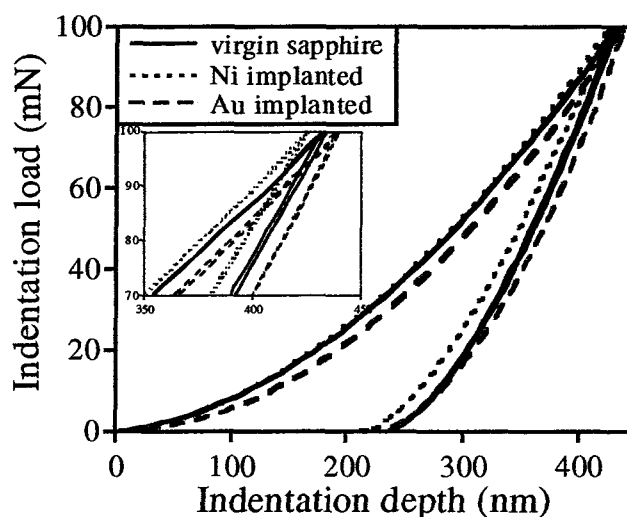

Fig. 2-1 Indentation load-displacement results for the plane of sapphire, virgin and modified with energetic Ni^{2+} and Au^{2+} ions, and deformed by a Berkovich-type indenter.
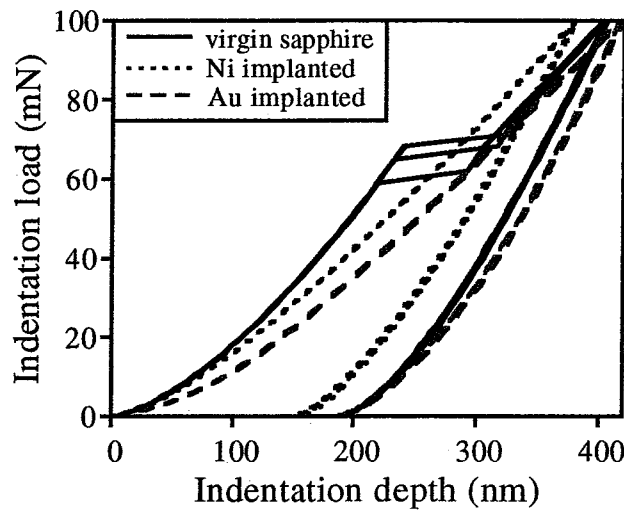
Fig. 2-2 Indentation load-displacement results for the plane of sapphire-virgin and modified with energetic Ni^{2+} and Au^{2+} ions deformed by a spherical tip indenter with nominally 2 μm radius.

[37], who attributed this effect to the location of the twin lamellae and consequently to the stage of the indentation process during which they are formed.

2.3.2. Load Partial-unload Indentation with Spherical Indenters

Load partial-unload tests were performed to determine the onset from elastic to plastic response of the ion-modified crystals. The typical results obtained by this particular tests [36] are illustrated in Fig. 2-3, which indicates minimal difference (5 nm) in the maximum penetration depth between the continuous and the partial-unload tests (compare Fig. 2-2 and Fig. 2-3). The implanted materials exhibit good reproducibility of the force-displacement response (typically less than 2% standard deviation).
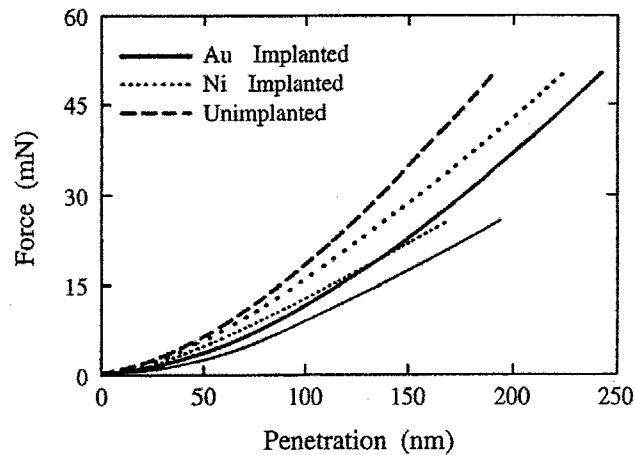

Fig. 2-3 Load partial-unload force-displacement data obtained with a spherical tip indenter nominally 2 m radius for unimplanted sapphire and modified with energetic Ni^{2+} and Au^{2+} ions.

24

For the unimplanted sapphire, the behavior of the pop-in event is as expected for an entirely elastic material, namely, that the partial-unloading data fall on the loading data points. Consequently, this approach enabled the contact pressure and modulus to be determined before and after the pop-in event. In the case of the implanted material, the onset of plastic deformation could be identified from the commencement of the splitting of the `loading points' from the `partial-unload points' (Fig. 2-3).

2.3.3. Contact Pressure

The plots of contact pressure versus depth of penetration for the three crystals (virgin, gold and nickel-implanted sapphire) at two different maximum loads (50 and 100 mN) are shown in Fig. 2-4a and 2-4b. The former, using the analysis developed by Field and Swain [38], were determined from the results illustrated in Fig. 2-3.

At the lower load, the virgin sapphire exhibits entirely elastic behavior achieving a maximum contact pressure of 27.2 GPa, whereas the implanted materials exhibit a slightly
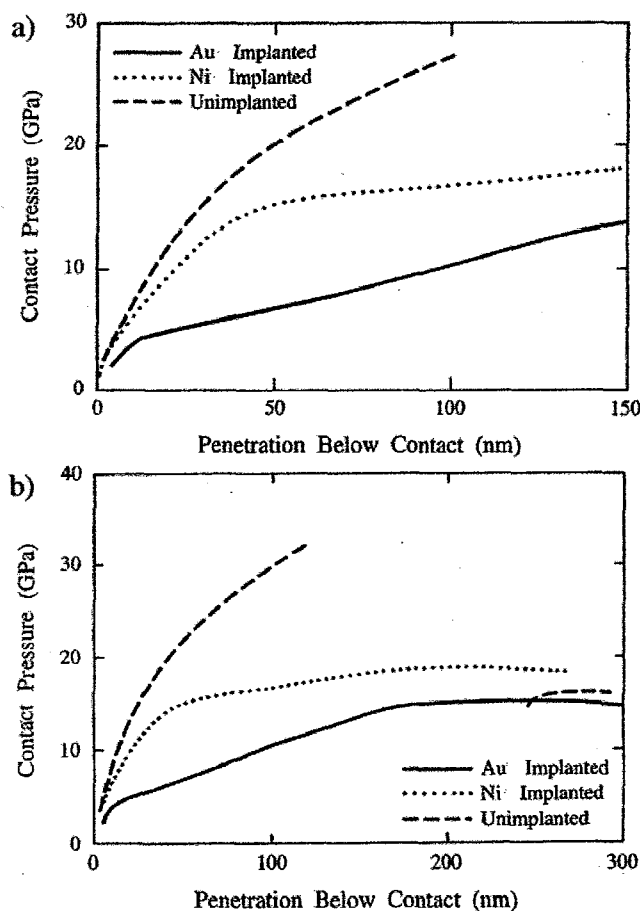

Fig. 2-4 Plots of contact pressure versus contact depth of penetration for the implanted and virgin sapphire obtained with a spherical tip indenter with nominally 2 m radius; taken for maximum indentation loads of 50 mN (a) and 100 mN (b).

less steep initial elastic response before plateauing at the yield stress at a contact pressure of 12-14 and 4-5 GPa for the crystals modified with nickel and gold ions, respectively. In both the implanted materials, the contact pressure continues to rise with further penetration beyond the onset of yield. The results for the 100 mN indentation tests confirm the observations made for the 50 mN tests but now show the contact pressure before and after pop-in for the plane of virgin Al_2O_3. The unimplanted material reached a maximum contact pressure of approximately 33 GPa at pop-in and thereafter stabilize at 16 GPa (Fig. 2-4).

In contrast, the nickel-modified aluminum oxide shows a continuously rising contact pressure to a depth of approximately 200 nm reaching a value of 18.6 GPa and thereafter slightly declining with further penetration. The data obtained for gold implanted Al_2O_3 appear to approach the value of the substrate (Fig. 2-4b).

2.3.4. Elastic Modulus

The variations of elastic modulus with depth of penetration into the virgin and ion-modified sapphire are shown in Fig. 2-5a. The obtained value measured by us is in fact the composite elastic modulus E*, given by equation (1)

$$1/E^* = (1 - v_1^2)/E_1 + (1 - v_2^2)/E_2 \qquad (1)$$

where v is Poisson's ratio and the subscripts refer to indenter (diamond E_1=1000 GPa, v_1=0.07) and specimen.

The results show a constant value for the virgin material with depth and a slightly lower value for Ni and significantly lower values for Au-implanted crystals. The evaluation of the surface roughness made prior to indentation reveals no significant difference between the implanted and the virgin areas. The elastic modulus of alumina crystal implanted with Au^{2+} ions increases uniformly with depth of penetration whereas for the material modified with Ni^{2+} species, it exhibits a gradual increase towards the value characteristic for bulk sapphire. The effective modulus of the virgin material displays minimal change when the pop-in occurs (Fig. 2-5b). There is less than a 10 GPa difference in the value of E* determined prior and after the pop-in event.

2.3.5. Contact Stress (pressure) Versus Contact Strain

Plots of mean contact stress versus contact strain (a/r, contact radius/indenter radius) for ion-implanted and virgin sapphire are shown in Fig. 2-6. The virgin material exhibits linear (elastic) behavior to pop-in as anticipated from the elastic relationship between mean contact pressure P_m and contact strain, namely;
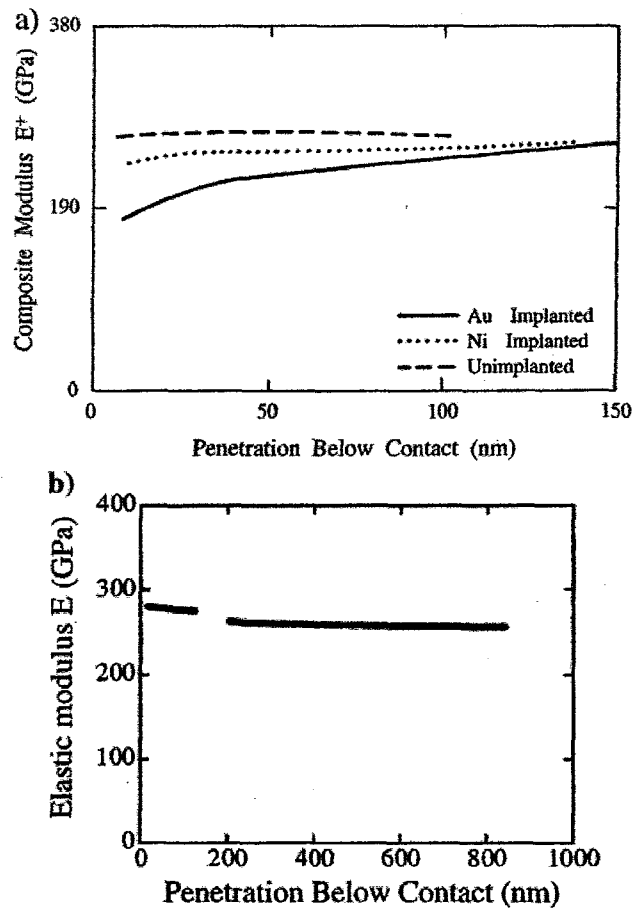
Fig. 2-5 Composite elastic modulus versus penetration for the unimplanted and ion-modified sapphire, determined for maximum indentation loads of 50 mN (a) and 500 mN (b).
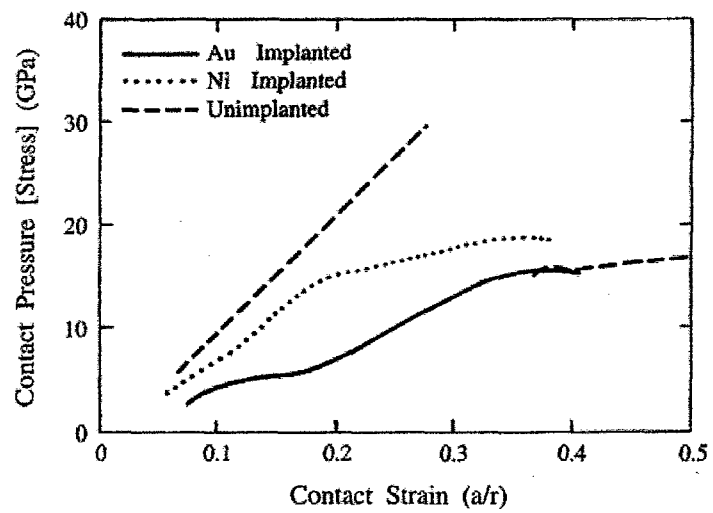

Fig. 2-6 Plots of mean contact pressure (or stress) versus contact strain for the unimplanted and ion-modified sapphire.

$$P_m = (3\pi / 8)E^*(a / r) \qquad\qquad (2)$$

The Ni-implanted material exhibits two distinct slopes prior to the onset of yielding. The initial slope is slightly lower than before yield, whereas a more complex response was registered for Al_2O_3 implanted with Au^{2+} ions.

2.3.6. AFM Obsevation of Residual Impressions of Sapphire

The indentation experiments marked residual impressions on the (1010) plane of sapphire even under loads of 100 mN, which is depicted in Fig. 2-7a. This residual impression show same pattern as what was described in a former work by Niihara et al.[37]. However, the maximum load of indentation is much lower, because the smaller radius of indenter (2 μm) is used in this study. The rhombohedra twinning is observed in our case which was confirmed to the deformation mechanism for (1010) plane [37]. The twin zone is located in the proximity of the contact surface and extend along the arrow directions which had been successfully predicted by using ERSS model [37].

The detail of the twinning area enlarged in Fig. 7b shows a regular saw-like shape. It was generated by the crystal structure transformation during the twin occurred. This observation of saw-like shape of twinning structure proved that the theoretical expectations in former work [37] were true. The present author believes that this is the first time of observation of twinning structure. When we enlarge the area with both twin and crack structure (the left and bottom of indentaiton impression), signigicant difference can be recognized for the irregular crystal deformation of crack and saw like structure of twin. The cross-sectional profile of twin area show a constant distance between two apex with the value of about 54 nm (see Fig. 2-8). The present author is still working on finding the mechanism of this twinning structure.

2.4. Discussion

The present observations with a spherical tip indenter for the virgin material are in excellent agreement with previous studies on the (1010) and other planes of sapphire by Swain and Whittling [39] and Nowak et al. [37]. In both instances, a pop-in event was observed irrespective of the surface indented whereas for polycrystalline alpha alumina no such behavior occurs [40]. Similar pop-in behavior has been reported by Page et al. [41] for
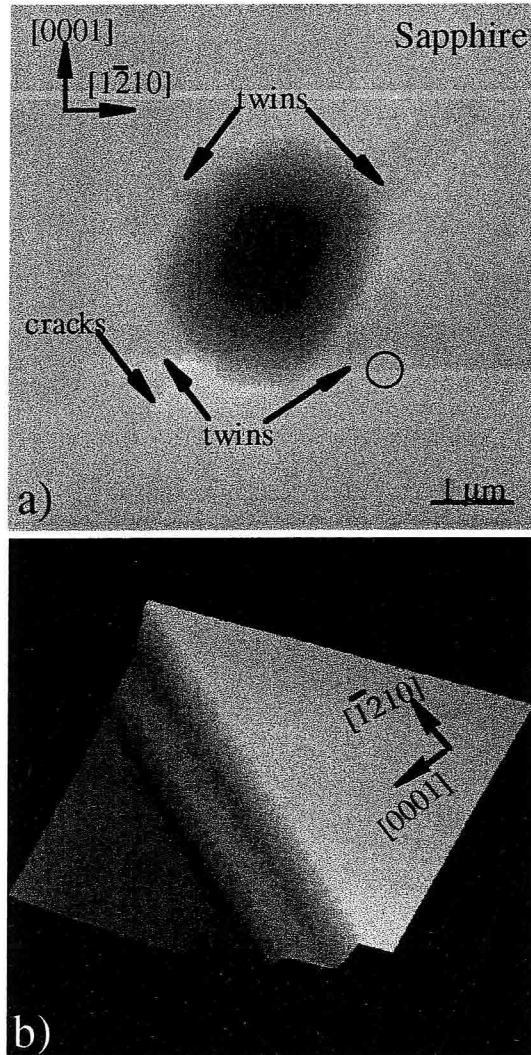
Fig. 2-7 AFM image of the residual impression in the plane (1010) of virgin sapphire obtained under the maximum load P_{max}=100 mN (a). Micrographs of the details of surface features near the twinned area (b).
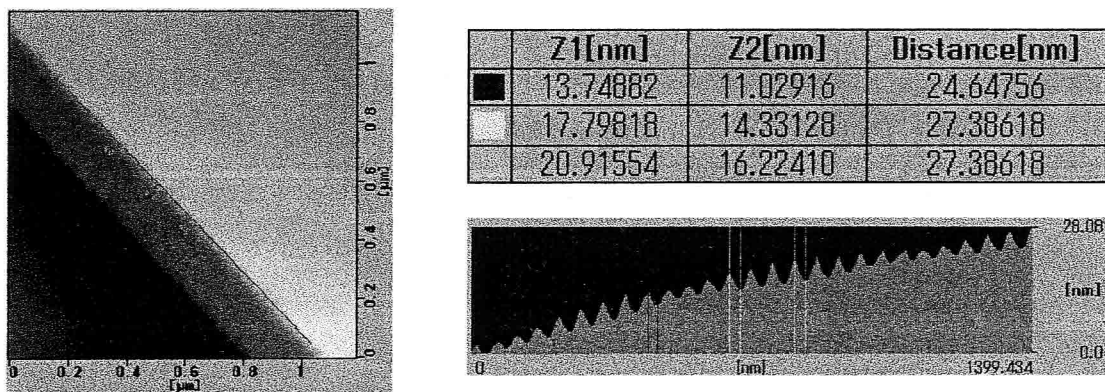

	Z1[nm]	Z2[nm]	Distance[nm]
■	13.74882	11.02916	24.64756
	17.79818	14.33128	27.38618
	20.91554	16.22410	27.38618

Fig. 2-8 AFM micrograph of the twin surface induce by the indentation impression on the (1010) plane of sapphire crystal together with the cross-sectional traces, highlighting the saw-liked structure of twin region.

sapphire using Berkovich indenters. The major difference between these studies of sapphire is the load for pop-in which is related to the effective radius of the indenter tip.

There are a number of other materials that exhibit similar pop-in like behavior during indentation. Dukino [42] observed such response in single crystalline hematite, Weppelmann et al. [43] saw such behavior in lithium niobate single crystals, and Williams et al. [44] have also seen such occurrence for single crystalline gallium arsenide. Only in the case of the lithium niobate, the pop-in was associated with cracking. In all other instances it appears to be associated with the nucleation of plastic deformation. For all the latter tests conducted with nano-indentation instruments there was virtually no evidence for a change in Young's modulus (E) before or after the pop-in event, whereas for the lithium niobate a significant drop in E was associated with pop-in. The present experiments (Fig. 5b) confirm the minimal change in E with the onset of pop-in.

Nowak et al. [37], Swain and Whittling [39] and earlier Farber et al. [45] investigating the indentation response of sapphire have observed twin lamellae in the vicinity of the residual impression and the surface features suggesting dislocation activity during the indentation process. Since two kinds of twins can be distinguished in sapphire, namely rhombohedral and basal (see Geipel, Lagerlof et al. [46, 47]), it is difficult to distinguish what type of twinning is responsible for the formation of the visible surface features. Page et al. [33] reported the presence of dislocations in sapphire at loads in excess of that to initiate pop-in with the Berkovich indenter. The location of the surface twin traces was reported by Nowak et al. [37] to correlate with the critical load for pop-in. An example of such twin traces maybe seen in the AFM image in Fig. 2-9a.

The onset of sub-surface shear failure beneath a spherical tip indenter is related directly to the magnitude of the stress acting in the slip/twinning systems appropriate for sapphire. An estimate of these stresses will be determined by resolving the shear stresses or determination of the so called critically resolved shear stresses (for details refer to [34] and [37]). The implication of such an analysis is that, provided there are pre-existing sessile dislocations, slip should initiate at the yield stress for the particular slip system at the location of the maximum shear stress. The present observations suggest that for virgin sapphire there is a paucity of defects and that a significant stress overload is required to achieve the theoretical shear strength or slip initiation at pre-existing, sites of high dislocation density or stress concentration. The sites do not coincide with the maximum resolved shear stress beneath the indenter. This situation leads to the scatter in pop-in loads observed for spherical indentation [37]. Once slip/twinning is initiated, the stress overload
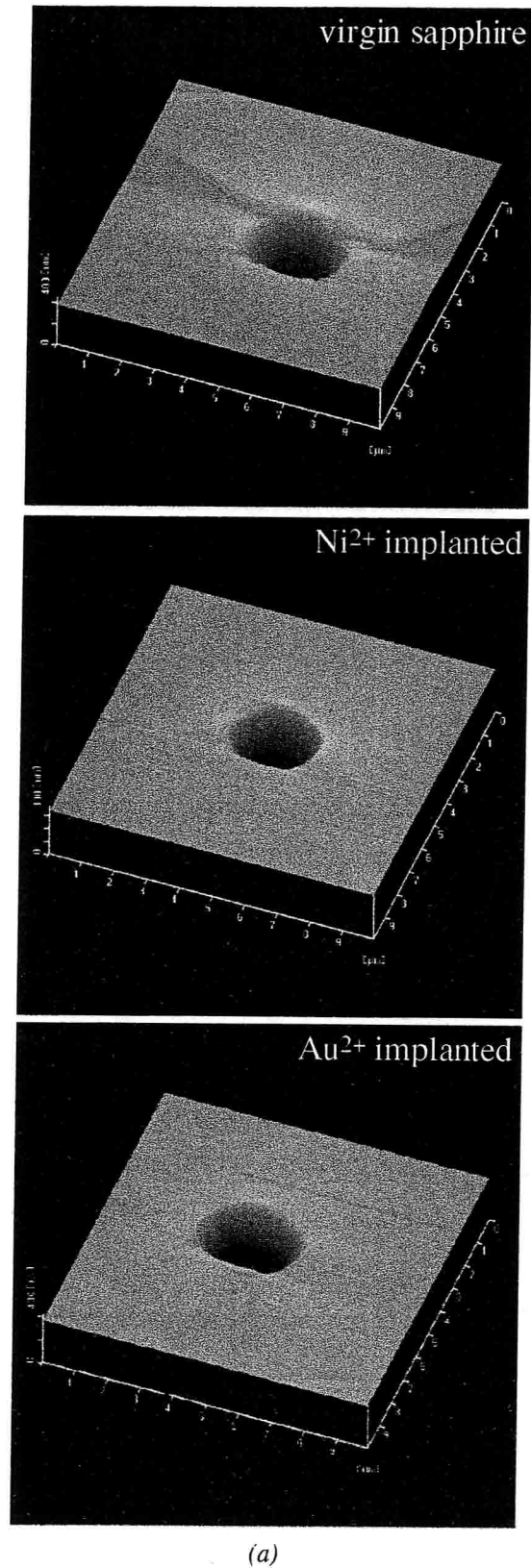
(a)

Fig. 2-9 Atomic force microscopy (AFM) images of the residual impressions in the (1010) plane of virgin sapphire and the crystal surface modified with energetic Ni2+ and Au2+ ions (a). Also attached are cross sectional traces of the residual impression (b) highlighting the surface traces and pile-up adjacent to the impression diameter of contact.
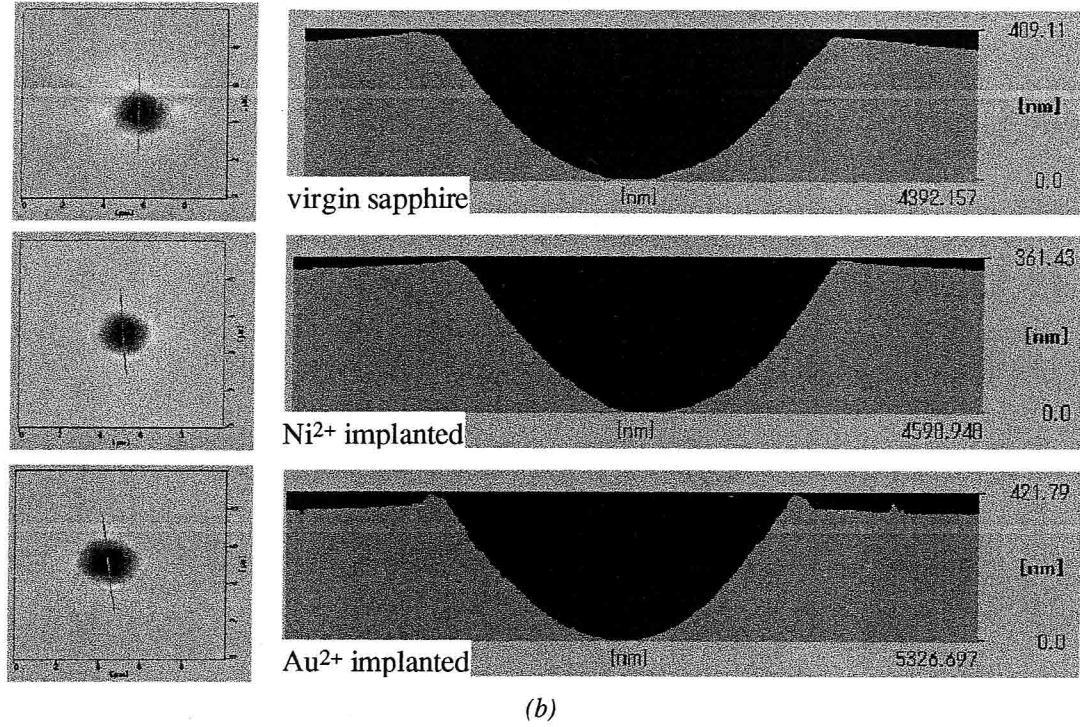
virgin sapphire

Ni^{2+} implanted

Au^{2+} implanted

(b)

Fig. 2-9 *(continued)*

leads to an avalanche of slip multiplication events. Further increases in force applied to the indenter result in a stable extension of the initiated slip. An estimate of the critical shear stress for the intiation of slip, assuming isotropic elastic behavior and a Huber von Mises yield criteria, is ~0.45 the mean contact pressure at the onset of yield [36]. The maximum contact pressure for the pop-in event (see Fig. 2-4b) equals 33 GPa implying an approximate yield stress of 15 GPa.

Previous studies of ion implanted sapphire [48] has established that electron, neutron and ion irradiation generate faults on the prismatic and (0001) basal planes with the population of such defects on the basal plane exceeding the prismatic loops by a factor of 20. In reviews of ion implantation of sapphire by McHargue [20] and Moncoffre [49], the displacements per atom (dpa) during ion irradiation, irrespective of species, is identified as a critical measure of crystal lattice disorder and amorphization at a specific temperature. At 300 K the extent of crystalline damage increases almost linearly until saturation occurs at ~10 dpa, whereas the onset of amorphization requires approximately 300 dpa. At 77 K amorphization of sapphire occurs at only ~3 dpa.

The dpa values calculated (TRIM-code) for our particular conditions of sapphire implantation with Ni^{2+} and Au^{2+} ions were up to 31 dpa and 120, respectively. The maximum occurred at a depth of 460 nm for the Au and 1000 nm for the Ni. The material modified by

32

nickel is well within the crystal damage dose, while the implantation with gold exceeds the saturation damage dose and is approaching the amorphization level [49]. In the latter case, small gold particles may have formed because of the exceptionally low solubility of Au in sapphire. Moreover, the excessive number of Frenkel pairs induced by bombardment with the very massive Au ions will result in forming numerous dislocation loops [48] and, in turn, sapphire will exhibit plastic behavior. On the other hand nickel, like most implantation species, may form vacancies and interstitials resulting in the development of compressive stresses within the implanted layer. A feature of the implantation is that lattice damage and implanted species reside beneath the surface forming a complex layered structure on the substrate. There is a relatively thin layer of near pristine material on the surface overlaying the lattice damaged zone. The contact mechanics modeling of such a two-layer system is complex because of the lack of knowledge of the properties of the damaged layer. For simplicity most studies consider the implanted layer as being uniform in properties and of a specific thickness, equivalent to the indentation of a film on a substrate. The determination of the yield response or hardness of such a layer is still an area of considerable controversy with many semi-empirical models available to deconvolute the influence the substrate influence on the measurements [50]. For spherical tip indenters, the situation is somewhat more complex than for pointed indenters because of the changing contact strain with penetration depth. The effect of elastic properties of the film and the influence of the substrate have been studied further. Recently Mencik et al. [51] have conclusively shown that the analysis of Gao et al. [52] is in excellent agreement with observations for a wide range of thin films of different thicknesses on various substrates.

The force-displacement data (Fig. 2-2) and resultant contact pressure versus depth of penetration (Fig. 2-4) show a smooth elastic-plastic transition for the Ni-implanted crystal in contrast to the virgin material. The onset of plastic deformation is difficult to pinpoint but appears to be in the range of 12-14 GPa (Fig. 2-4). With increasing penetration the contact pressure rises to a maximum of 18-19 GPa at an indentation depth of ~200 nm and thereafter it declines. The maximum value is 1.5-2 GPa higher than for virgin sapphire. The contact diameter at maximum contact stress equals to 1.3m which coincides with the location of the concentration peak of Ni species (TRIM-code calculations, see Experimental).

AFM images of the impression in the   plane of sapphire implanted with Ni^{2+} ions (Fig. 2-9a) show a complete absence of twin lamellae in the vicinity of the indentation in the virgin crystal but also significant differences in the form of the pile-up of material about the residual impression. The modulus of the surface modified with nickel is somewhat lower

than that of the virgin sapphire as is evident in the force-displacement and modulus versus depth of penetration curves (Fig. 2-2 and Fig. 2-5). These observations suggest that yield occurs at a resolved shear stress of ~5.5 GPa. The elastic modulus E* (Fig. 2-5) shows a gradual increase with depth of penetration or contact radius normalized to implanted layer thickness asymptotically approaching the virgin material at sufficient depth of penetration.

Previous studies of ion implanted sapphire by transmission electron microscopy have clearly established the formation of sessile dislocations on the primary slip planes [20]. With the presence of such dislocations the contact stress field, upon reaching a sufficiently high shear stress, is able to cause the motion of these dislocations resulting in plastic flow without overload or pop-in as with virgin material. As noted by previous investigators [48] the presence of lattice damage results in a larger lattice resistance to dislocation motion and hence a higher contact pressure to achieve continued plastic flow.

The Au-implanted region exhibits a marked softening with again a smooth transition from elastic to plastic response and a contact pressure at yield in the vicinity of only 5 GPa or a yield stress of only 2.25 GPa (Fig. 2-4). Once yield has occurred, the contact pressure appears to remain almost constant for some tens of nanometers before slowly rising towards the bulk value. A somewhat similar effect is observed for the elastic modulus which commences much lower than for Ni-implanted sapphire but asymptotically approaches, with increasing contact depth the value characteristic for the virgin material. The much higher dpa values obtained for the Au-implanted material indicate that such a damaged structure is much easier to deform plastically. AFM observations of the residual impressions in the Au-implanted sapphire show a significant pile-up adjacent to the circle of contact (Fig. 2-9b)

The behavior of E* versus contact radius-normalized to the depth of implanted layers for ion-modified Al_2O_3 crystals is shown in Fig. 2-10. Following the approach by Mencik et al. [51] and fitting Gao's relationship [52] to our results, we estimated the E* value of the implanted layer by projecting the data to zero contact radius. Consequently, they appeared to equal 232 and 151 GPa for sapphire modified with Ni^{2+} and Au^{2+} ions, respectively. The latter value agrees with the value quoted by Oliver and McHargue [53] for sapphire amorphized by ion implants at 77 K.

Comparison of the present spherical indentation results with previous experiments by pointed indenters show several similarities. Hioki et al. [14, 15] found a 10-25% increase in the hardness of sapphire implanted with Ni ions at 300 K (E=300 keV, fluence=1015-1015 cm-2), while at higher doses the hardness fell to about 60% of the virgin sapphire value when evaluated with a Knoop indenter. Further, O'Hern et al. [32] reported that nano-
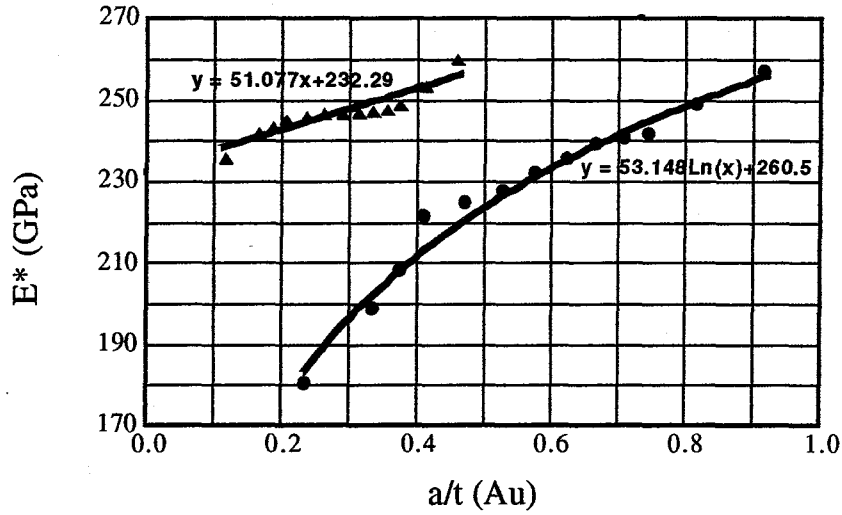
Fig. 10 Composite elastic modulus versus contact radius normalized to the implanted layer thickness, a/t.

indentation results taken for amorphized sapphire were initially only 50% of the values obtained for virgin sapphire (for the first 50 nm of indentation depth) and increased asymptotically (for higher indentation depth) to the level characteristic for unimplanted crystal. Both these sets of observations are similar to the results of the present study. Moreover, SEM observations by Hioki et al. [16] performed for the implanted and amorphized sapphire displayed pile-ups adjacent to the contact area for Vickers indentations, similar to our AFM images reported for sapphire modified with Au^{2+} ions.

2.5. Conclusions

In order to verify the influence of the cluster-level dispersiods on the crystal structure control, the difference on deformation behavior of the virgin and modified sapphire was studied in the present chapter. The second phase was introduced into matrix sapphire on the cluster-level by suing ion implantaion method. The results can be summarized as following:

The present observations show that contact studies with small spherical tipped indenters are able to distinguish the influence of ion implantation resulting in mild and more severe damage of sapphire crystal-lattice.

The unimplanted alumina is characterized by a sharp pop-in of plastic deformation at contact stresses well in excess of the steady-state hardness of the material. The twinning structure occured on the (1010) plane of the sapphire shows a regular saw-like structure, which has been observed on the first time using the atomic force microscopy.

The cluster-level dispersed second phases (Ni^{2+} and Au^{2+} ions) give the matrix crystal a

smooth transition from elastic to plastic behavior. This difference in mechanical properties (especially for the Ni^{2+} implanted material) is associated with the presence of cluster-size dispersiods able to move at a critical shear stress whereas for the virgin material the paucity of such dislocations requires a significant overload to initiate such deformation.

The local topography of the region close to the residual impression reflects the difference in initiation of deformation, with the unimplanted material showing traces of twins and the Au-implanted area local pile-ups at the edges of contact. The elastic modulus is slightly reduced for alumina crystals bombarded with Ni^{2+} ions and changes significantly for aluminum oxide modified with Au^{2+} ions.

All the above results show that the cluster-sized dispersiods would make a critical effect on the structure and then mechanical properties of the matrix material. It means that the fracture manner like twinning and crack can be modified by cluster-level composite technique, which is quite important for applications of ceramic materials in industry.

References

1   E.W.J. Mitchell, J.D. Rigden and P.D. Townsend, Phil. Mag. 5, 1013-1027 (1960)

2   R.S. Wilks. J. Nucl. Mater. 26, 137-173 (1968)

3   G.P. Pells. AERE Report No. R9359 Atomic Energy Research Establishment, Harwell, UK (1979)

4   G.W. Arnold, G.B. Krefft and C.B. Norris, Appl. Phys. Lett. 25, 540-542 (1974)

5   G.B. Krefft and E.P. EerNisse, J. Appl. Phys. 49, 2725-2730 (1978)

6   M.D. Rechtin, Radiat. Eff. 42, 129-136 (1979)

7   A. Turos, H.J. Matzke, P. Rabette, Phys. Stat. Sol. A64, 565-572 (1981); C.J. McHargue, H. Naramoto, B.R. Appleton, C.W. White and J.M. Williams, Proc. Mater. Res. Soc. 7, 147-153 (1982)

8   C.J. McHargue and C.S. Yust, J. Am. Ceram. Soc. 67, 117-123 (1984)

9   H. Naramoto, C.W. White, J.M. Williams, C.J. McHargue, O.W. Holland, M.M. Abraham and B.R. Appleton, J. Appl. Phys. 54, 683-698 (1983)

10 H. Naramoto, C.J. McHargue, C.W. White, J.M. Williams, O.W. Holland, M.M. Abraham and B.R. Appleton, Nucl. Instr. Meth. Phys. Res. 209/2106, 1159-1161 (1983)

11 G.C. Farlow, C.W. White, C.J. McHargue and B.R. Appleton, Proc. Mater. Res. Soc. 27, 395 (1984)

12 G.C. Farlow, P.S. Sklad, C.W. White and C.J. McHargue, J. Mater. Res. 5, 1502-1519 (1990)

13 T. Hioki, A. Itoh, S. Noda, H. Doi, J. Kawamoto and O. Kamigato, J. Mater. Sci. Lett. 3, 1099-1101 (1984)

14 T. Hioki, A. Itoh, M. Okubo, S. Noda, H. Doi, J. Kawamoto and O. Kamigato, J. Mater. Sci. 21, 1321-1328 (1985)

15 T. Hioki, A. Itoh, S. Noda, H. Doi, J. Kawamoto and O. Kamigato, Nucl. Instr. Meth. Phys. Res. B7, 521-525 (1985)

16 T. Hioki, A. Itoh, S. Noda, H. Doi, J. Kawamoto and O. Kamigato, Nucl. Instr. Meth. Phys. Res. B39, 657-664 (1989)

17 P.J. Burnett and T.F. Page, J. Mater. Sci. 19, 5524-5545 (1984)

18 P.J. Burnett and T.F. Page, J. Mater. Sci. 20, 4624-4646 (1985)

19 C.J. McHargue, G.C. Farlow, C.W. White, J.M. Williams, B.R. Appleton and H. Naramoto, Mater. Sci. Eng. 69, 123-127 (1985)

20 C.J. McHargue, Nucl. Instr. Meth. Phys. Res. B19/20, 797-804 (1987)

21 P.S. Sklad, J.C. McCallum, C.J. McHargue and C.W. White, Nucl. Instr. Meth. Phys. Res. B46, 102-106 (1990)

22 L. Romana, P. Thevenard, B. Canut, G. Massouras, R. Brenier and L. Brunel, Nucl. Instr. Meth. Phys. Res. B56, 94-97 (1990)

23 C.J. McHargue, P.S. Sklad, C.W. White, J.C. McCallum, A. Perez and G. Marest, J. Mater. Res. 6, 2160-2177 (1991)

24 C.J. McHargue, P.S. Sklad, C.W. White and G.C. Farlow, J. Mater. Res. 8, 2145-2159 (1991)

25 C.J. McHargue, M.E. O'Hern, C.W. White and M.B. Lewis, Mater. Sci. Eng. A115, 361-367 (1989)

26 W.R. Allen and D.F. Pedraza, Nucl. Instr. Meth. Phys. Res. B59/60, 1159-1162 (1991)

27 Y. Chen, M.M. Abraham, D.F. Pedraza, Nucl. Instr. Meth. Phys. Res. B59/60, 1163-1166 (1991); T. Miyano, T. Matsumae, H. Yoko-o, Y. Andoh, M. Kinchi, M. Satou, Nucl. Instr. Meth. Phys. Res. B59/60, 1167-1172 (1991)

28 R. Nowak, K. Ueno, M. Kinoshita, Fracture Mechanics of Ceramics, vol. 10, in: R.C. Bradt (Eds.), Plenum, New York 155-174 (1992)

29 S.J. Bull and T.F. Page. J. Mater. Sci. 26, 3086-3106 (1991)

30 D. Newey, M.A. Wilkins, H.M. Pollock, J. Phys. E: Sci. Instrum. 15, 119-124 (1982); J.B. Pethica, R. Hutchings, W.C. Oliver, Phil. Mag. A 48, 593-606 (1983)

31 J.B. Pethica, R. Hutchings and W.C. Oliver, Nucl. Instr. Meth. Phys. Res. 209/210, 995-1000 (1983)

32 M.E. O'Hern, C.J. McHargue, C.W. White and G.C. Farlow, Nucl. Instr. Meth. Phys. Res. B46, 171-17 (1990) 5.

33 T.F. Page, W.C. Oliver and C.J. McHargue, J. Mater. Res. 7, 469-473 (1991)

34 R. Nowak, M. Sakai, J. Mater. Res. 8, 1068-1078 (1993); R. Nowak, M. Sakai, Acta metall. et materialia 42, 2879-2891 (1994)

35 W. Ensinger and R. Nowak, Nucl. Instr. Meth. Phys. Res. B80/81, 1085-1090 (1993)

36   M.V. Swain, Mater. Sci. Eng. A 253, 160-166 (1998)

37   R. Nowak, T. Sekino, S. Maruno, K. Niihara, Appl. Phys. Lett. 68, 1063-1065 (1996); R. Nowak, T. Sekino, K. Niihara, Phil. Mag. A74, 171-194 (1996)

38   J.S. Field and M.V. Swain, J. Mater. Res. 8, 293-300 (1993)

39   M.V. Swain and M. Whittling, Surf. Coat. Technol. 77, 528-533 (1995)

40   A. Bushby and M.V. Swain, Plastic Deformation of Ceramics. In: R.C. Bradt, C. Brookes and J. Routbort Editors, NY: Plenum (1995), p. 161.

41   T.F. Page, C. Warren and C.J. McHargue, J. Mater. Res. 7, 450-473 (1992)

42   R.D. Dukino and M.V. Swain, J. Am. Ceram. Soc. 75, 3299-3304 (1992)

43   E.R Weppelmann, J.S. Field, M.V. Swain, AUSTCERAM 92, Proc Int.Ceramic Conf. Melb. Vic. August 1992, in: M.J. Bannister (Eds.), CSIRO Aust. 2 (1992) 839-844.

44   J.S. Williams, J.S. Field and M.V. Swain, Proc. MRS Symp. 308, 571-579 (1993)

45   B.Y. Farber, S.Y. Yoon, K.P.D. Lagel-f, A.H. Heuer, Z. Metallkd., Teitschrift f-r Metallkunde 84, 426-430 (1993)

46   T. Geipel, K.P.D. Lagerl-f, P. Pirouz and A.H. Heuer, Acta Metall. Mater. 42, 1367-1372 (1994)

47   K.P.D. Lagerl-f, Plastic Deformation of Ceramics, In: R.C. Bradt, C. Brookes, J. Routbort, NY: Plenum (1995), p. 217.

48   S.J. Zincle, Proc. MRS Symp. 128, 271-279 (1988)

49   N. Moncoffre, Nucl. Instr. Meth. Phys. Res. B59/60, 1129-1142 (1991)

50   M. Wittling, A. Bendavid, P.J. Martin and M.V. Swain, Thin Solid Films 270, 283 (1995)

51   J. Mencik, D. Munz, E. Quandt, E.R. Weppelmann and M.V. Swain, J. Mater. Res. 12, 2475-2484 (1997)

52   H. Gao, C.H. Liu and J. Lee, Int. J. Sol. Struct. 29, 2471 (1992)

53   W.C. Oliver and C.J. McHargue, Thin Solid Films 153, 185 (1987)

Chapter 3

Preparation and Mechanical Properties of Al_2O_3-Cr_2O_3
Solid Solutions by Using Powder Metallurgical Process

The Al_2O_3-Cr_2O_3 solid solutions with different amount of chromia were prepared by the conventional hot-pressing method. The mixture was prepared by conventional powder metallurgical process. Even Al_2O_3-Cr_2O_3 solid solutions with high content of chromia was also studied in this work, the author focused much on the case of the less amount of Cr_2O_3 (0.1–1.0 mol%) solid solutions. The present work confirmed that the lattice parameter of the Al_2O_3-Cr_2O_3 solid solution scaled with the content of Cr_2O_3. The lattice constant of the material containing less than 0.6 mol% Cr_2O_3 remained unchanged while it increased linearly with increasing content of Cr_2O_3 for the chromia-rich solution, as predicted by Vegard's law. The solid solution with 0.4 mol% of Cr_2O_3 exhibited the maximum fracture strength. The registered variations of the mechanical properties were caused by the relocation of Cr_2O_3 within the matrix grain and nano particles inside of grains.

3.1 Introduction

Although ion bombardment can inject the second phase into matrix material on the level of cluster-size, this process has some disadvantages. The distribution of the implanted species are not homogenous. The energetic ions are not stopped at same depth but a Gaussain distribution inside the matrix because of the random collision and cascade processes, which means that the concentration of implanted ions depends on different depth from the surface. Therefore, ion bombardment process has been mostly treated as a surface modification process [1-4]. For the case of ceramics, ion bombardment process is not best candidate process to disperse the second phase on the level of cluster size.

The solid-solution of Al_2O_3-Cr_2O_3 has been thoroughly investigated in the past decade due to its complete solid solubility and the superior mechanical properties such as hardness, strength and wear resistance compared to alumina [5-6]. Chromium oxide (Cr_2O_3) appears to be a refractory material with high melting point which is appreciated due to its high temperature oxidation resistance [7]. Cr_2O_3 and α-Al_2O_3 crystallize in the corundum type of crystal structure and their Al^{3+} and Cr^{3+} ions posses a similar radius [8]. The above mentioned coincidence of lattices and ionic radii makes it possible to obtain the perfect,

continuous solid solution of the discussed materials at temperatures as high as 900°C [9]. Consequently, Roy and Barks [10] studied phase equilibrium of Al_2O_3-Cr_2O_3 under the pressure of 1000 bar while the temperature varied from 400 to 1200°C. Moreover, the variation of the lattice parameter [11], elastic properties [12], sintering kinetics [13] and migration of grain boundaries [14] were already investigated. A number of reports were also devoted to the improvement of mechanical properties of the Al_2O_3-Cr_2O_3 solid solution [15-17] while Ghate and Davies [18,19] focused on the application of Al_2O_3-Cr_2O_3 system for cutting tools and refractory materials.

Based on our research results of nanocomposites, it was not difficult to find that the smaller dispersiods we want, the less additions of second phase we added. A dozen percent of second phase are generally added for microcomposites in contract to several percent for nanocomposite. In this chapter, we mainly focus on the case of small amount of Cr_2O_3 addition (less than 1.0 mol%) to get the cluster-level controlled structure. Surprisingly, there are no works on the Al_2O_3-Cr_2O_3 solid solution systems with a small content of Cr_2O_3 (below 1.0 mol%) except the interesting report by Hollenberg and Gordon [20] concerning on creep properties of 1.0 mol% Cr_2O_3 doped Al_2O_3.

The examination of our materials was accomplished using the depth-sensing indentation technique, being capable to determine hardness, Young's modulus as well as to provide the information on the elastic-plastic behavior in the very small volume of the material [21]. The nano-indentation technique has been already used for metallic materials [22,23], and recently proved to be successful in determining the properties of Al_2O_3 single crystals [24,25]. It is commonly considered to be a proper tool to characterize thin films to avoid the substrate effect [26]. The reports concerning nano-indentation of ceramics with fine polycrystalline ceramics structure are rather scarce. The works by Mayo *et al.* who has reported the nano-indentation results of nanocrystalline TiO_2 and ZnO as the example of such a research [27,28].

In this chapter, the Al_2O_3-Cr_2O_3 solid solutions with different amount of chromia were prepared by the conventional hot-pressing method. The present work confirmed the influence of Cr_2O_3 additions on the microstructure and the mechanical properties. The obtained results are discussed together with the data obtained by the classic hardness measurements, as well as conventional bending test. Furthermore, X-ray diffraction, atomic force microscopy and scanning electron microscopy were used to determine the surface microstructure, while the Cr_2O_3 content was evaluated by transmission electron microscopy with EDX capabilities.

3.2 Experimental

3.2.1 Sample preparation

In order to prepare the material, we mixed a proper amount of powders of α-Al_2O_3 (AKP-53, average particle diameter of 0.3 μm) and two kind of Cr_2O_3 (average particle diameter are 3.0 and 0.85 μm.). The small size of Cr_2O_3 was selected for the case of low Cr_2O_3 addition in order to obtain the homogeneous powder mixture. The experimental procedure is schematically summarized in Fig. 3-1. The latter was subsequently wet-milled in ethanol solvent for 24 hours using alumina balls. The obtained slurry was dried in air and dry-milled to avoid agglomeration of the components. We select the particle size smaller then 100 μm by putting the powder through a sieve. Further, the mixture was packed into carbon dies and then hot-pressed (from 1400°C to 1600°C) for 1 hour in argon atmosphere under the applied pressure of 30 MPa. The sintered disks were about 44mm in diameter and 5mm in the thickness. The hot-pressed bodies were cut, ground and polished in rectangular bars with 40×4×3 mm (JIS R1601) in size for bending test.

3.2.1 Properties Evaluation

Relative density

Density of the specimen was measured by the Archimedes method using toluene or distilled water at room temperature. The relative density was determined by dividing the apparent density by the theoretical density which was calculated by using the lattice parameters obtained by X-ray analysis.
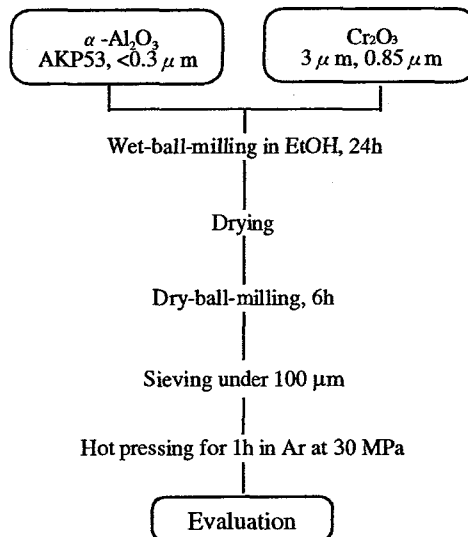
Fig. 3-1 Schematic illustration of experimental procedure.

Characterization

Crystalline phases of sintered specimens were determined by X-ray diffractometry (50 kV, 150 mA, RU-200B, Rigaku Co. Ltd.). X-ray diffraction (XRD) pattern was taken using CuKα radiation (l = 0.15418 nm). The 2θ angle scanning rate was 4°/min, and the identification of phases present in specimens was referred to JCPDS (Joint Commit of Power Diffraction Standards) data. The lattice parameters of the obtained material were determined by X-ray diffraction partition measurement, with high purity silicon (99.99%) used as the internal standard. The lattice constant was calculated for each sample using least square fitting method. The density of our materials was calculated by using the lattice parameters obtained by X-ray analysis.

Young's modulus

The specimens (3×4×42 mm) were coated by a carbon painting on one side in order to act as an electrode and then suspended on two thin tungsten wires in correspondence of the nodal points. Flexural vibrations were generated by electrostatic force and resonance frequencies were determined by using an oscilloscope. Young's modulus, E, was calculated by using the following Eq. 3-1,

$$E = 0.9465 \times \frac{M \cdot f^2}{w} \left(\frac{l}{t}\right)^3 \left\{1 + 6.59\left(\frac{t}{l}\right)^2\right\} \tag{3-1}$$

where M, w, t, l and f are the mass, the width, the thickness, the length of the specimen and the resonance frequency obtained, respectively.

Hardness

Hardness, Hv, was measured by a Vickers indentation (AVK-2, Akashi Co. Ltd.), and calculated by the following Eq. 3-2,

$$Hv = \frac{2P\sin(\theta/2)}{d^2} \tag{3-2}$$

where P is the applied load, d is the diagonal of the indentation measured by optical microscope ($d=2a$) and θ is 136° which is the angle comprised between the two opposite faces of the pyramidal indenter. Load was applied and held constant during a period of 15 seconds.

42

Fracture strength

The tensile surface was ground and polished with 9 μm, 2 μm and finally 1/2 diamond pastes. The tensile edges on the tensile surface were beveled to reduce the effect of edge cracks. Three-point bend testing (span of 30 mm) was used to determine the flexural strength using a mechanical testing machine (Autograph AG-10TC, Shimadzu Co. Ltd.) under a cross-head displacement speed of 0.5 mm/min. The strength, σ, was given by the following Eq. 3-3,

$$\sigma = \frac{3FL}{2bt^2} \qquad (3\text{-}3)$$

where F (N) is a fracture load with obtained by three point bending testing, L is the span of 30 mm in this case and b and t are the width and the thickness of specimen, respectively.

Fracture toughness

Fracture toughness was evaluated by the Vickers indentation microfracture (IF) method using a micro Vickers diamond indenter based on the standard of JIS-R 1607. Two loads (P) of 98 and 196 N were used to investigate the effects of indentation load on the fracture toughness. The loads were applied for 15 second on the polished surface of specimen at room temperature by a Vickers hardness tester (AVK-C2, Akashi Co. Ltd., Tokyo, Japan). Six indents were made at each indentation load. The fracture toughness, K_{IC}, was calculated by the following Eq. 3-4 given by Niihara [29],

$$K_{IC} = 0.203(c/a)^{-3/2} a^{1/2} Hv \qquad (3\text{-}4)$$

where c and a are the length of median crack and half length of the diagonal of the indentation, respectively,. Hv is the Vickers hardness.

Nanoindentation

The monolithic Al_2O_3 and Al_2O_3-Cr_2O_3 solid solutions were tested using the ultra micro-indentation system (UMIS 2000, CISRO) equipped with pointed diamond indenter of Berkovich type. The variations of the indentation load, hardness and Young's modulus with depth of penetration were registered for maximum indentation loads from 50 to 500 mN. At least five independent measurements were completed for each indentation load. The considerable effort was made to reduce the noise caused by vibration as well as temperature

and humidity variation during the measurement. The residual indentation impressions have been examined using the atomic force microscope (AFM, Nanoscope II, Nano Instrument Inc.) which allowed us to register the profile of the deformed surface.

Microstructure

Microstructure was characterized by optical microscopy, scanning electron microscopy (SEM). SEM specimens were prepared by chemical etching with NaOH at 400°C for 1 min. Microstructure of the composites was evaluated by SEM (Model S-5000, Hitachi Co., Japan). Grain size and its distribution were analyzed from SEM photographs by using a commercial software package of image analysis (NIH image, National Institute of Health, Bethesda). About 1000 grains per microstructure were used for statistical analysis to obtain the grain thickness and length for each grain. Transmission electron microscopy (TEM) was used at an accelerating voltage of 200 kV to observe the distribution of Cr_2O_3 particles. TEM samples were prepared by mechanically grinding down to 150 mm, then drilling by using ultrasonic to obtain 3mm diameter discs. The obtained thin discs were dimpled and finally thinned by Ar ion beam.

3.3 Results and Discussions

3.3.1 Al_2O_3-High Content Cr_2O_3 Solid Solutions

The lattice constants a and c for the solid solutions show a linear increment in accordance with the amount of the Cr_2O_3 additions as depicted in Fig. 3-2. This increment obeys Vegard's rule which was agree to Rossi and Lawrence's report [12]. The Young's modulus linearly
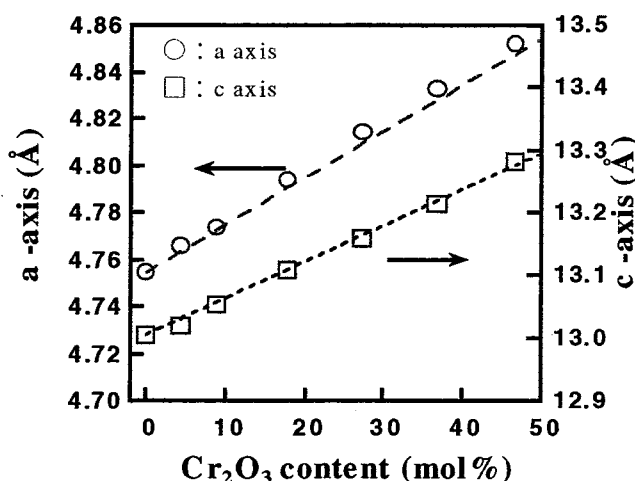
Fig. 3-2 Variation of lattice parameters of Al_2O_3-Cr_2O_3 solid solution as a function of Cr_2O_3 content.
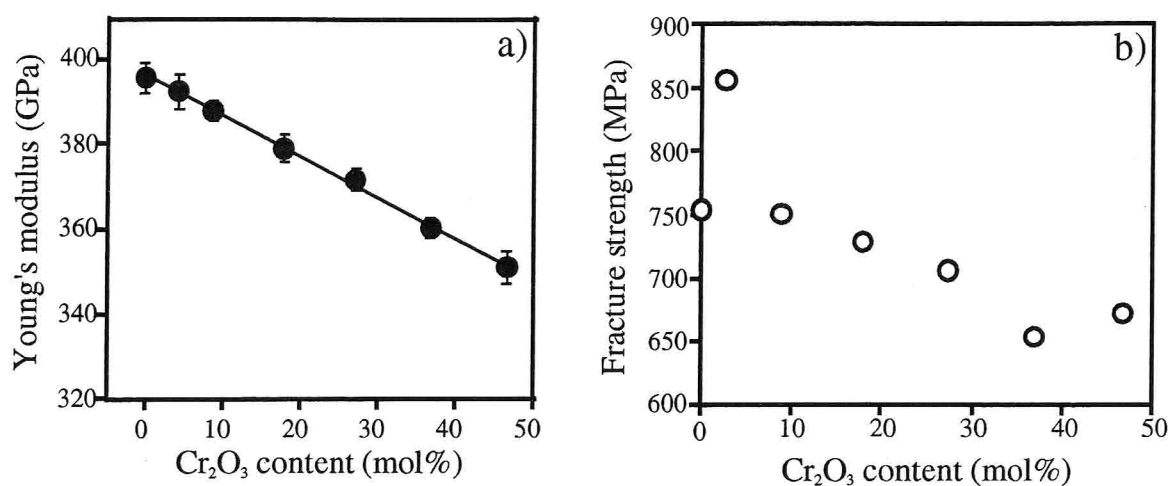
Fig. 3-3 Young's modulus and fracture strength with Cr_2O_3 content for Al_2O_3-Cr_2O_3 solid solutions.
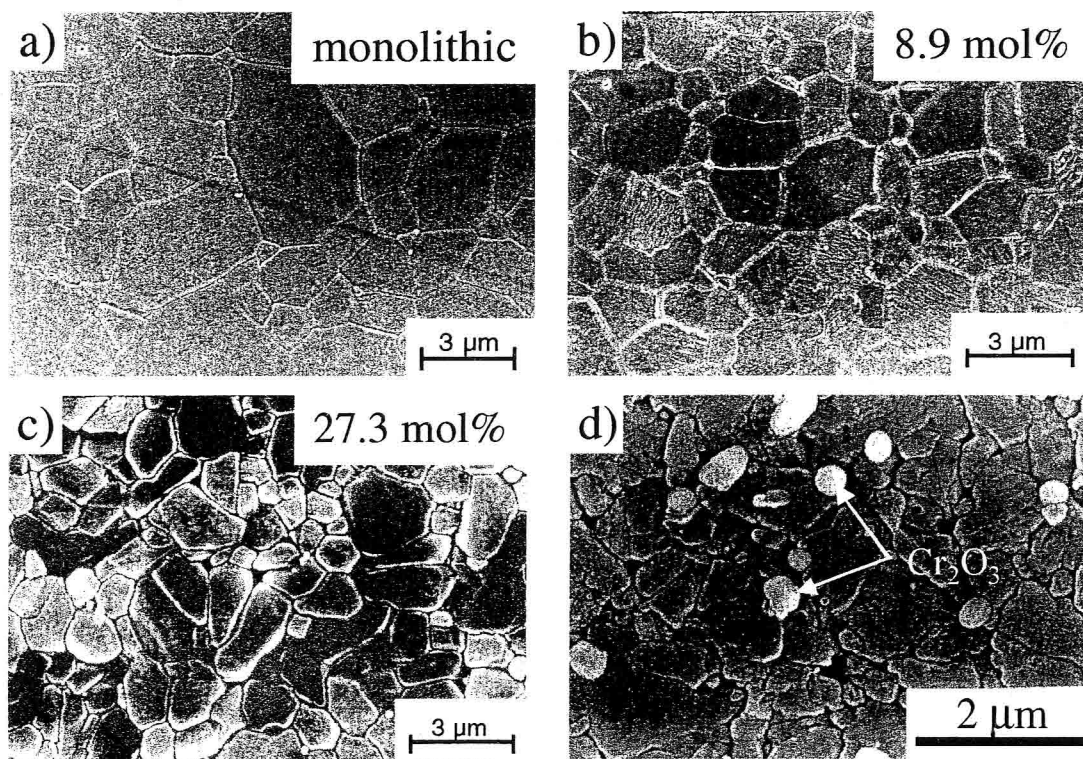
Fig. 3-4 SEM micrographs of Al_2O_3-Cr_2O_3 solid solutions with different Cr_2O_3 addition (a)-(c) sintered at 1500°C, as well as Al_2O_3-46.7 mol% Cr_2O_3 solid solution (d) sintered at 1400°C for 1h.

decreased with increasing the mole fraction of Cr_2O_3, which can expected from the increase of inter-atomic distance caused by bigger Cr^{3+} ion which replaced the smaller Al^{3+} ions by making solid solution (See Fig. 3-3a).

Fig. 3-3b shows the variation of fracture strength with variation of Cr_2O_3 content for Al_2O_3-Cr_2O_3 solid solution. The strength of the Al_2O_3-Cr_2O_3 increased up to about 850 MPa while the Cr_2O_3 content are less than 10 mol%. Such a high strength was considered mainly because of effect of the decrease in the grain size. In the case of more Cr_2O_3 added, the decrease of the Young's modulus and the relative density result in the fracture strength down in spite of the matrix grain size reduced.

The SEM micrograph of the morphology of matrix grains are depicted in Fig. 3-4. One can easy recognize that the grain size was inhibited with increasing the content of Cr_2O_3 additions (compare with Fig. 3-4a, 3-4c, 3-4c). However, we can observe the white precipitated Cr_2O_3 particles for the Al_2O_3-Cr_2O_3 materials with the highest content of Cr_2O_3 (Fig. 3-4d).

In a short summary, though the grain size has been inhibited, however, we can not find any effect caused by nano/cluster-level composition on Al_2O_3-Cr_2O_3 solid solutions with the high content of Cr_2O_3 addition.

3.3.2 Al_2O_3-Low Content Cr_2O_3 Solid Solutions

3.3.2.1 Microstructure and mechanical properties of Al_2O_3-Cr_2O_3 solid solutions

The lattice constants a and c of hexagonal structure of the Al_2O_3-Cr_2O_3 solid solution depend on the content of chromia (see Fig. 3-5). It is worth noting that the value of lattice parameters increase with rising amount of Cr_2O_3, which suggests that Al_2O_3 and Cr_2O_3 compounds form a solid solution at the experimental conditions we selected (temperature=1400°C, pressure=30 MPa). Starting with the value of 0.6 mol% of Cr_2O_3 content, the lattice parameters increase linearly according to the Vegard's law (Fig. 3-5). The lattice parameters remains unchanged for the Al_2O_3-Cr_2O_3 solid solution containing less than 0.6 mol% of Cr_2O_3, since within the indicated interval of Cr_2O_3 concentration, the amount of Cr_2O_3 is too small to significantly affect on the lattice of Al_2O_3. Indeed, Rossi and Lawrence [12] already confirmed the formation of the solid solution for higher contents of Cr_2O_3 by measuring the lattice constant of Al_2O_3, which supports our conclusion.

Moreover, we found the density of Al_2O_3 varying linearly with the Cr_2O_3 content, when the relative density for the specimen exceeds 99.3%, and it strongly depends on whether the
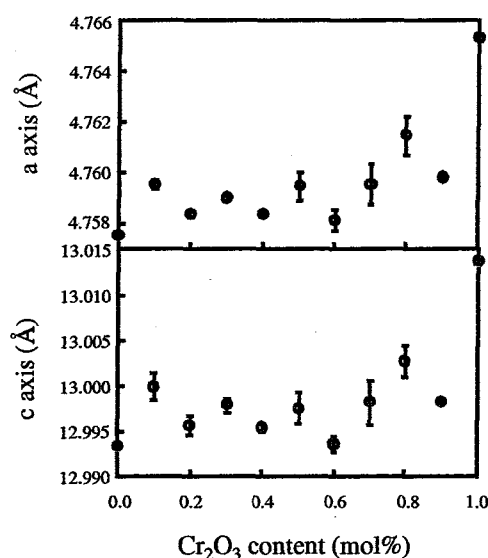
Fig. 3-5 Variation of lattice parameters of Al_2O_3-Cr_2O_3 solid solution as a function of Cr_2O_3

amount of Cr_2O_3 exceeds 0.6 mol% or not. One should notice that the difference in density between monolithic Al_2O_3 and Al_2O_3-Cr_2O_3 solid solution of 1.0 mol% chromia is very small ($\Delta r \approx 0.01$ g/cm³). Consequently, a limited addition of Cr_2O_3 does not involve significant modification of the crystal structure what is reflected in tiny changes of the relative density.

The microscopic observations (SEM) of the morphology of matrix grains were carried out to investigate the structure of Al_2O_3-Cr_2O_3 solid solution. Although Hasselman et al. [30] have already reported that Cr_2O_3 appears to act as a grain-growth inhibitor for high contents of Cr_2O_3, we found that the grain size increases with increasing content of Cr_2O_3 (Figs. 3-6a and 3-6c). Moreover, we observed both the inter- and intra-granular fracture modes for our Al_2O_3 and Al_2O_3-Cr_2O_3 solid solutions, while the greater fraction of the inter-granular fracture occurred for the high strength specimens (see Figs. 3-6d-f). We also found the increase of average grain size of Al_2O_3-Cr_2O_3 solid solutions containing more than 0.4 mol% Cr_2O_3 measured on SEM micrographs (Fig. 3-7). EDS (Energy Dispersive Spectroscopy) analysis of chromium element performed at both inter- and intra-granular regions of the prepared materials proved that Al_2O_3-Cr_2O_3 solid solution with 1.0 mol% Cr_2O_3 contains Cr_2O_3 mainly in the grain boundary area, and Cr_2O_3 was not detected inside of the matrix grains (Fig. 3-8). The decrease of strength for the materials with Cr_2O_3 addition higher than 0.4 mol% maybe explained by the migration of Cr^{3+} into matrix and the increase of the grain size (see Fig. 3-7 and Fig. 3-8).

The dependence of fracture strength on the content of Cr_2O_3 in Al_2O_3-Cr_2O_3 solid solution is shown in Fig. 3-9. The fracture strength remains unchanged for the material containing less than 0.3 mol% of Cr_2O_3. Even when the content of Cr_2O_3 is too small to

47
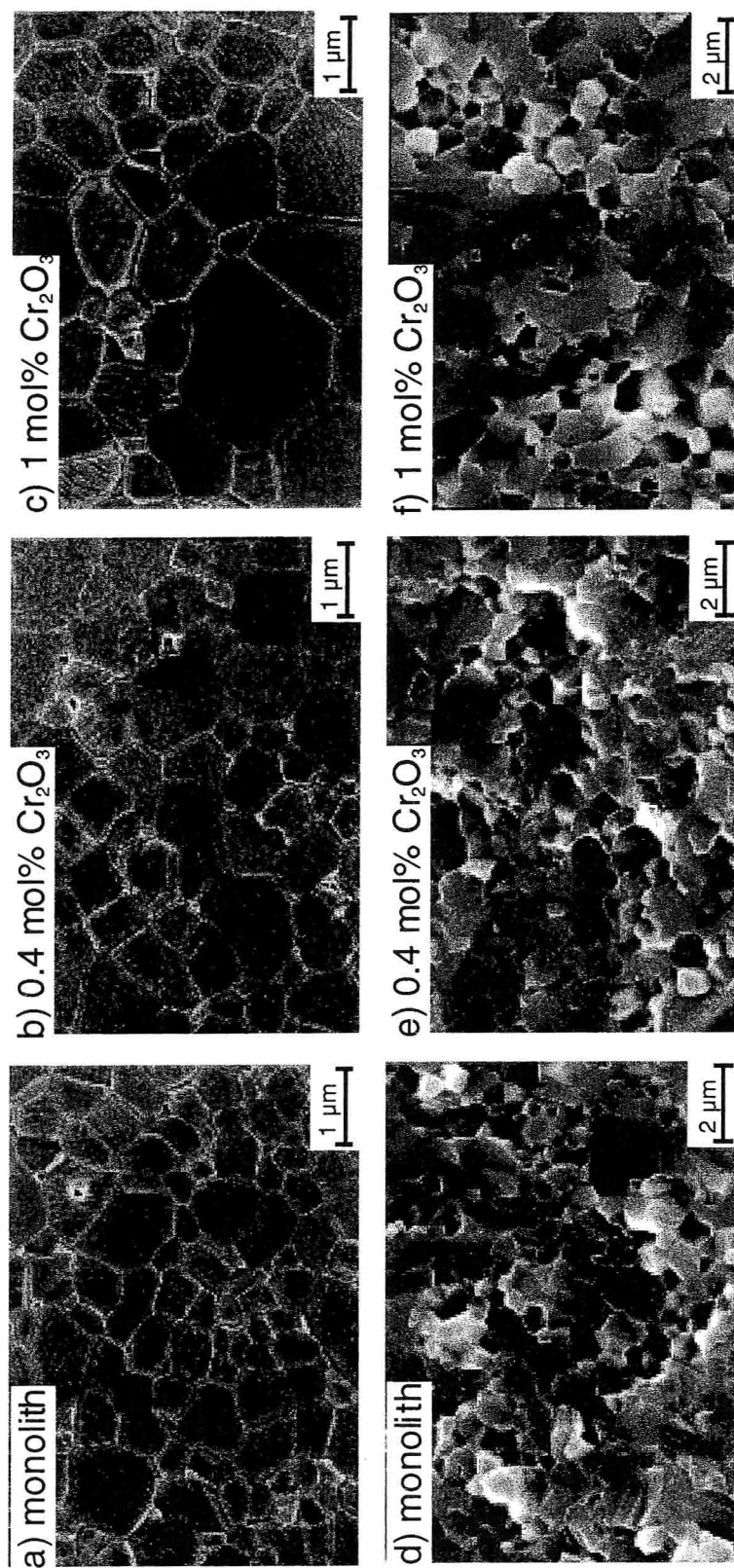
Fig. 3-6 SEM micrographs of the Al_2O_3 (a), (d) and Al_2O_3-Cr_2O_3 solid solution containing 0.4 mol% (b), (e) and 1 mol% (c), (f) of Cr_2O_3.
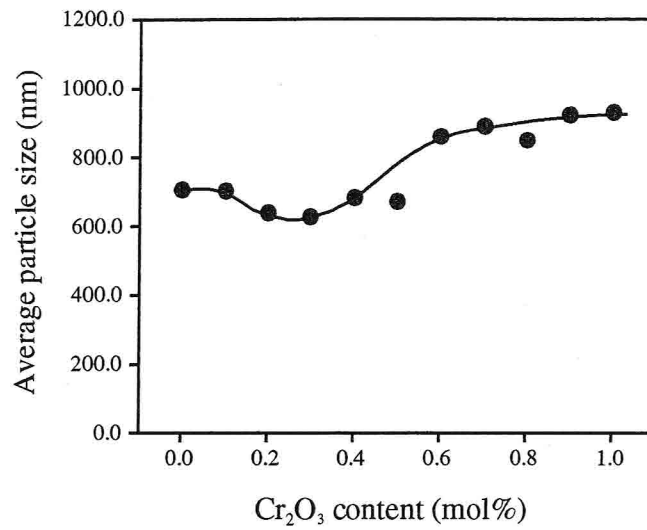
Fig. 3-7. Average particle size of Al_2O_3-Cr_2O_3 solid solution deduced from SEM images.
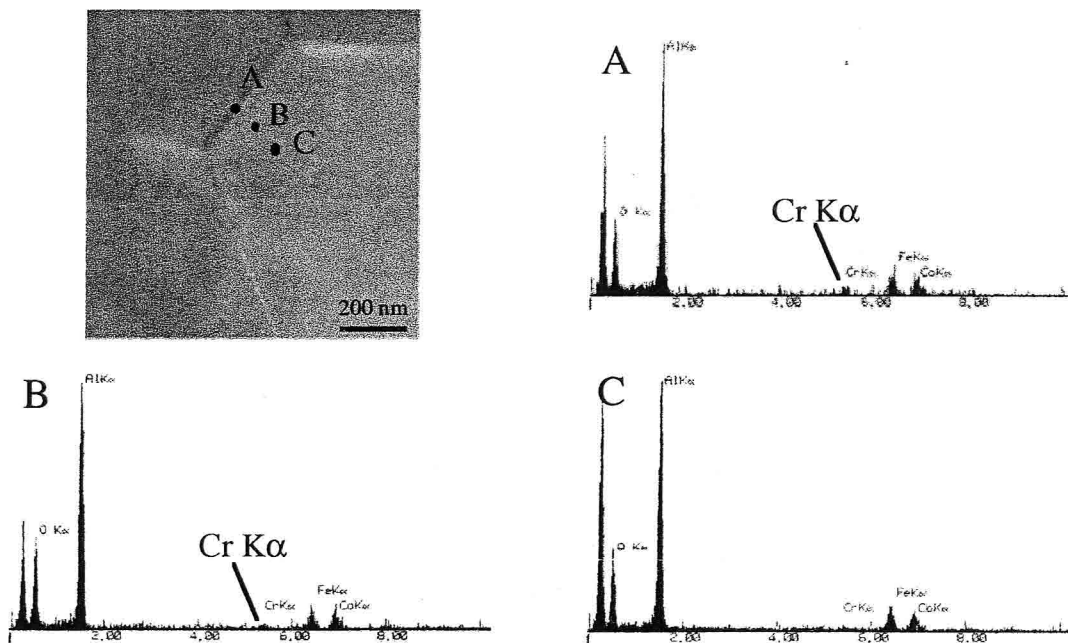

Fig. 3-8 TEM image of the sintered Al_2O_3-Cr_2O_3 solid solution and EDS-spectra corresponding to the analytical points denoted by (A), (B) and (C).

affect the material structure, the fracture strength increased due to doping with Cr_2O_3 (see maximum strength for 0.4 mol% Cr_2O_3 - Fig. 3-6). The above mentioned change of fracture strength was due to the grain-boundary effect which occurs in a similar way as in the case described by Ardell [30]. Further, the compressive stress is believed to arise when the larger Cr^{3+} ions substitute the smaller Al^{3+} within the grain boundary region (note that ionic radiuses of Al^{3+} and Cr^{3+} are 0.68 Å and 0.76 Å, respectively). It could result in the interaction between grains, and might affect the fracture strength (refer to [31] and to our result - Fig. 3-9). In the case of low content of chromia, the solid solution was detected only within the grain boundary region. The higher fracture strength is due to the above-mentioned limited amount of solid solution and smaller grain size. Al_2O_3-Cr_2O_3 solid solution with 0.4 mol% Cr_2O_3 possess the highest strength, which is believed to be caused by Cr^{3+} residing in the
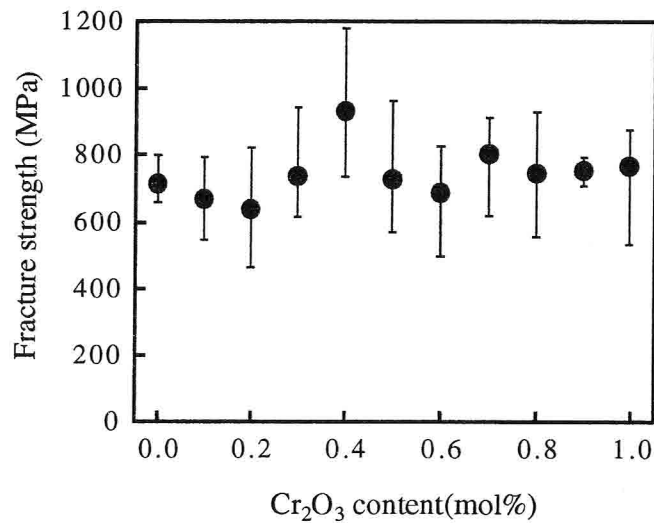
Fig. 3-9 Variation of fracture strength with the Cr_2O_3 content for Al_2O_3-Cr_2O_3 solid solutions.
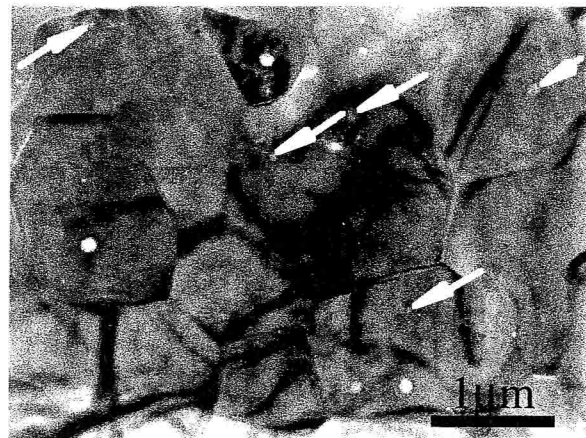
Fig. 3-10 TEM micrograph of Al_2O_3-Cr_2O_3 solid solution hot-pressed for 1h at 1400°C.

grain boundary (see Fig. 3-8). Separately, we can find nano-sized Cr_2O_3 particle inside the Al_2O_3 grains by TEM observations as shown in Fig. 3-10. In such a case, Cr_2O_3 will create considerable stress in the Al_2O_3-Cr_2O_3 solid solution with high content of Cr_2O_3, which can also increased material's strength which known as nanocomposite strengthing mechanism.

3.3.2.2 Nano-indentation experiments

Typical examples of the indentation load-depth hysteresis loops registered for 0.5 and 1 mol% Al_2O_3-Cr_2O_3 solid solutions as well as monolithic alumina are depicted in Fig. 3-10. The hysteresis loops obtained for Al_2O_3-Cr_2O_3 solid solution are of similar shape as those obtained for monolithic Al_2O_3. The curves are smooth and regular, without sudden pop-in which indicate either twining or pressure induced phase transformation as observed for Al_2O_3 crystals [25]. The maximum indentation depth h_{max} in Al_2O_3-Cr_2O_3 solid solution is higher than in monolithic Al_2O_3, while it is considerably smaller when the solution contains 1 mol% of Cr_2O_3 (Fig. 3-11). The solid solution created in the boundary region affects the indentation results. It is worth to notice that the residual indentation depth h_r remains unchanged for the Al_2O_3-Cr_2O_3 solid solution with a low content of chromia, but it is smaller for the solid solutions with 1.0 mol% of Cr_2O_3. The limited addition of Cr_2O_3 which locates itself in the grain boundary region affects the elastic properties of our material (see the initial part of the loading cycle of the indentation curves – Fig. 3-10). When Cr_2O_3 forms the solution inside the matrix grain, the deformation properties of our materials are changed because the internal stress created by Al^{3+} ions replacement by bigger Cr^{3+} (see e.g. the case
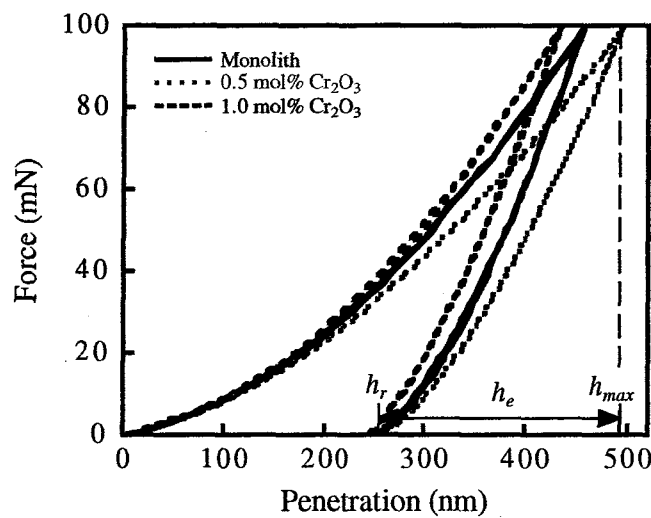
Fig. 3-11 Typical indentation hysteresis loops obtained for monolithic Al_2O_3 and Al_2O_3-Cr_2O_3 system containing 0.5 and 1 mol% of Cr_2O_3.

of solid solution with 1.0 mol% content of Cr_2O_3). All of this suggests nothing but that plastic properties of the composite depend on the location of Cr_2O_3 within the volume of the grain.

The conventional hardness calculated from the depth-sensing indentation data (hardness calculated from indentation contact geometry at a maximum load P_{max} - Fig. 3-11) varied with indentation load which is a common effect obtained for a range of ceramics (indentation size effect). There were no variations in hardness of Al_2O_3-Cr_2O_3 solid solution when the content of chromia was lower than 0.7 mol% (Fig. 3-12), since for such an interval of low Cr_2O_3 concentrations, chromia is mainly located in the grain boundary region, as discussed in the previous section.

The higher hardness observed when concentration of Cr_2O_3 exceeds 0.8% (Fig. 3-12) is associated with an indicated changes in the structure inside the grain. As it was already mentioned, we believe that for higher Cr_2O_3 content, Cr_2O_3 is not located exclusively near the grain boundary, but it also exists inside the matrix crystallites. The latter effect results in hardening of the materials and it agrees with the conclusions by Bradt [16] derived for the Al_2O_3-Cr_2O_3 solid solution with the Cr_2O_3 content considerably higher than in our case.

The AFM micrographs of the residual indentation impressions in Al_2O_3 and Al_2O_3 doped with 1 mol% Cr_2O_3 as well as the cross-section depth profiles of indentation marks are depicted in Fig. 3-13. The impressions appear to posses a defined shape without traces of the radial cracks, which suggests completely plastic behavior of the deformed material (Fig. 3-13), in contrast to brittle indentation response of many ceramics (e.g., sapphire crystal) [21].

The similar size of impressions observed for both monolithic alumina and chromia-added Al_2O_3, is consistent with the coincidence of indentation hysteresis loops shown in Fig. 3-11. The latter proves that low addition of Cr_2O_3 to Al_2O_3 allows us to modify exclusively the elastic characteristics of the material, while high content of Cr_2O_3 changes both elastic and plastic properties. The identical indentation depth registered by AFM cross-section profile (Fig. 3-13) and indentation curves (Fig. 3-12) confirms our conclusion.

3.4 Conclusions

High content of Cr_2O_3 addition shows the possibility of microstructure control through inhibiting the grain size development during the sintering process. However, no affect caused by nano/cluster-level composition on Al_2O_3-Cr_2O_3 solid solutions was found.
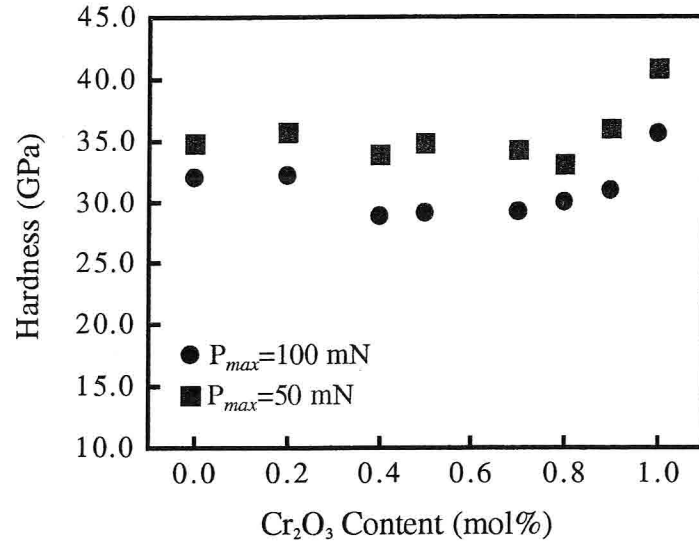
Fig. 3-12. Conventional hardness of Al_2O_3-Cr_2O_3 composites as a function of the content of Cr_2O_3. The hardness was calculated using the maximum indentation depth.
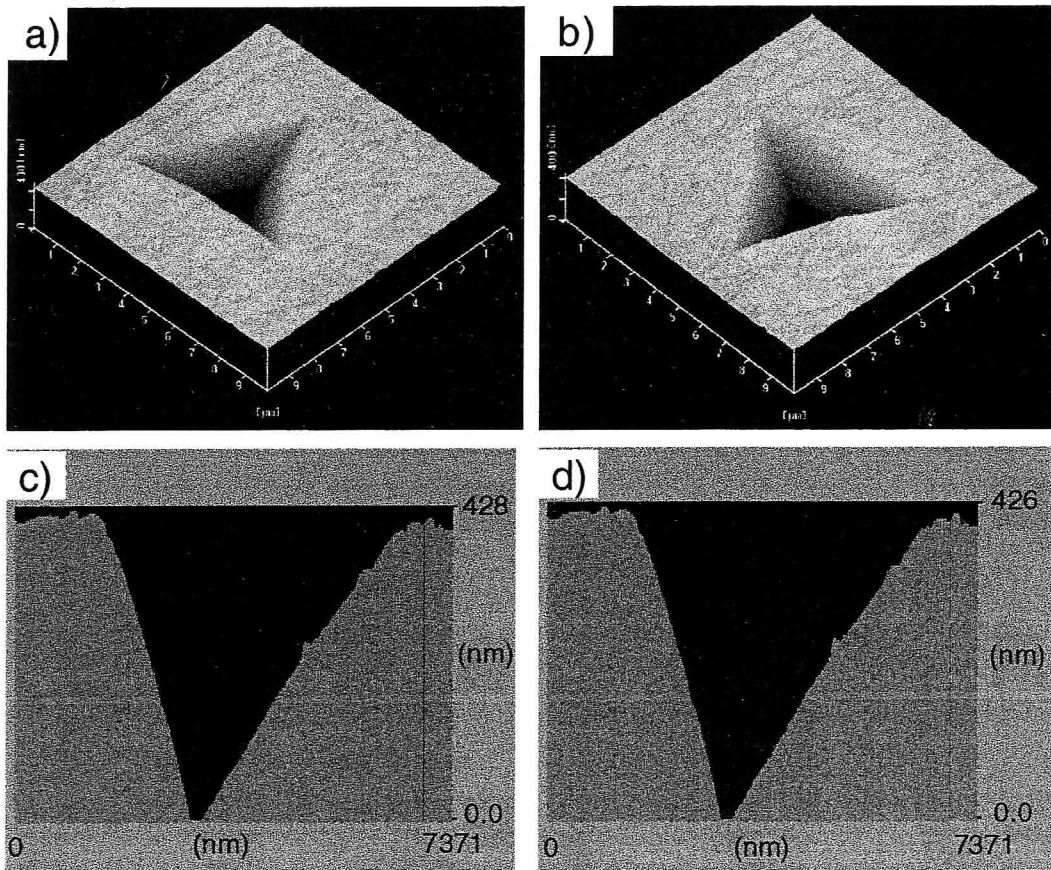

Fig. 3-13 Typical AFM micrographs of the indentation impression (P_{max}= 300 mN) and the depth-profile of the Al_2O_3 (a), (c) and Al_2O_3-Cr_2O_3 solid solution containing 1 mol% of chromia (b), (d).

53

The investigation of the Al_2O_3-Cr_2O_3 solid solution with a small content of Cr_2O_3, which were produced using hot-pressing method, allowed us to conclude on the changes of structure and mechanical properties which were caused by the Cr_2O_3 doping.

The formation of a solid solution of Al_2O_3-Cr_2O_3 was assured based on the measurements of the Al_2O_3 lattice constants. We found that the lattice parameters of our material increased in the Cr_2O_3 content exceeding 0.6 mol%. Further, we found the increase in grain size when Cr_2O_3 was located inside the Al_2O_3 matrix grains. The maximum strength of the material was achieved for Al_2O_3 containing 0.4 mol% of Cr_2O_3.

The nano-indentation results proved that the small addition of chromia can affect the mechanical properties of Al_2O_3. Hardness of Al_2O_3-Cr_2O_3 solid solution was higher when the content of Cr_2O_3 exceeds 0.7 mol%. In particular, the material with Cr_2O_3 within the grain volume was found to be hardened (its plastic properties were affected).

Microstructure observations show that low addition of Cr_2O_3 can affect the matrix structure on the level of the nano-size, with a incline distribution on the grain boundary. The large particle size of starting powder is the main barrier on fabricating the cluster-level composite which caused the inhomogeneous solid solution inside matrix. These experimental results and discussion suggest that a new processing is required in order to fabricated the completely homogeneous solid solutions in the Al_2O_3-Cr_2O_3 systems. This conclusion must be true for other material systems.

References

1 C.W. White, G.C. Farlow, C.J. McHargue, P.S. Sklad, M.P. Agelini and B.R. Appleton, Nucl. Instr. and Meth., B7/8, 473 (1985)

2 C.J. McHargue and C.S. Yust, J. Am. Cer. Soc., 67, 117 (1984)

3 K.O. Legg, J.K. Cochran, H.F. Solnick-legg and X.L. Mann, Nucl. Instr. and Meth., B7/8, 535 (1985)

4 P.J. Burnett and T.F. Page, Mater. Res. Soc. Symp. Proc., 27, 401 (1984)

5 E. Ryshkewitch, in: Oxide Ceramics, Academic Press, New York, 1960.

6 P. Schwarazkopf and R. Kieffer, in: Redractory HardMetals, Springer-Verlag, Berlin, 1953

7 W. H. Giltzen, in: Alumina as a ceramic Material, American Ceramic Society, Columbus, OH, 1970

8   W.D. Kingery, H. K. Bowen, D.R. Uhlmann, in: Introduction to Cereamics, John Wiley & Sons Inc., 1976

9   E. N. Bunting, J. Res. Nat. Bur. Stand. , 6, 947-949 (1931)

10   D.M. Roy and R.E. Barks, Nature Phys. Sci., 235, 118-119 (1972)

11   M. Watanabe, T. Hirayama, M. Yoshinaka, K. Horita and O.Yamaguchi, Mater. Res. Bul., 31, 861-868 (1996)

12   L.R. Rossi and W.G. Lawrence, J. Am. Ceram. Soc., 53, 604-608 (1970)

13   S. V. Raman, J. Mater. Sci., 22, 3161-3166 (1987)

14   S.C. Han, D.Y. Yoon, M.K. Brun, Acta. metall. mater., 43, 977-984 (1995)

15   T. Arahori and E. D. Whitney, J. Mater. Sci., 23, 1605-1609 (1988)

16   R.C. Bradt, J. Am. Ceram. Soc., 50, 54-55 (1966)

17   K. Aratani and Y. Tamai, Yogyo-Kyokai-Shi, 89, 480-487 (1981)

18   B.B. Ghate et al, Ceram. Bul., 54, 210-215 (1975)

19   T.J. Davies, H.G. Emblem, C.S. Nwobodo, A.A. Ogagu and V. Tsantzalou, J. Mater. Sci., 26, 1061-1068 (1991)

20   G.W. Hollenberg and R.S. Gordon, J. Am. Ceram. Soc., 1973, 56, 140-147

21   J.S. Field and M.V. Swain, A simple predictive model for spherical indentation, J. Mater. Res., 1993, 8, 297-306

22   J. B. Pethica, R. Hutchings, and W.C. Oliver, Hardness measurement at penetration depths as small as 20 nm, Phil. Mag., A48, 593-606 (1983)

23   W.C. Oliver and G.M. Pharr, J. Mater. Res., 7, 1564-1583 (1992)

24   R. Nowak, T. Sekino and K. Niihara, Phil. Mag. A, 74, 171-194 (1996)

25   R. Nowak, T. Sekino, S. Maruno and K. Niihara, Appl. Phys. Lett., 68, 1063-1065 (1996)

26   R. Nowak, C.L. Li and S. Maruno, J. Mater. Res., 12, 64-69 (1997)

27   M.J. Mayo, R.W. Siegel, A. Narayanasamy and W.D. Nix, J. Mater. Res., 5, 1073-1082 (1990)

28   M.J. Mayo, R.W. Siegel, Y.X. Liao and W.D. Nix, J. Mater. Res., 7, 973-979 (1992)

29   K. Niihara, R. Morena, and D. P. H. Hasselman, J. Am. Ceram. Soc. 65,C-116 (1982)

30   A.J. Ardell, Acta. Metal., 20, 61-71 (1970)

31   D. P. H. Hasselman, R. Syed and T.-Y. Tien, J. Mater. Sci., 20, 2549-2556 (1985)

Chapter 4

Preparation of Al_2O_3-Cr_2O_3 Mixed Powder by Coprecipitation Technique

The homogeneously dispersed powder mixture of Al_2O_3 and 1.0 mol% Cr_2O_3 was prepared by using the coprecipitation process under the selected optimum conditions. The powders was examined by means of in-situ high temperature X-ray diffraction, differential thermal analysis and electron microscopy which enabled us to conclude on the phase components and structure of the mixture. We witnessed the complex phase transformation in Al_2O_3 during the calcination process, in contrast to Cr_2O_3. The crystallization process which occurred at various calcination temperatures was also examined. The powder calcinated at 1200°C shows a homogeneous size distribution and a better sinterability can be expected.

4.1 Introduction

The improvement of the thermal shock resistance and strength of polycrystalline ceramic remains for two decades as a main interest of researchers. The above mentioned properties are essential for the application of ceramic materials in gas turbines and aerospace structures. The studies on strengthening of Al_2O_3 by adding Cr_2O_3 have been performed as early as in 1966 by Kirchner and co-workers [1-3]. Al_2O_3 and Cr_2O_3 possess similar properties, typical for refractory materials with high melting point, and they are appreciated due to their high temperature oxidation resistance [4]. Moreover, Al_2O_3 and Cr_2O_3 have the same crystal structure of corundum type, and the ionic radius of Al^{3+} and Cr^{3+} is similar [5]. The apparent coincidence of the lattices and ionic radii of Al_2O_3 and Cr_2O_3 makes it possible to obtain the perfect, continuous solid solution of the discussed materials at temperatures as high as 900°C [6].

In previous chapter, the improvement of the mechanical properties of the Al_2O_3-Cr_2O_3 solid solution with a low amount of Cr_2O_3 - which was prepared by powder mixture process, was discussed. It was found that the dispersion of Cr_2O_3 could significantly affect the properties of the sintered material. All of these enhancements were verified due to the micro- or nano-level structure control or modification [7]. However, the powder metallurgical process was recognized not to be enough for preparing the homogeneous solid solutions.

Consequently, it seems that the dispersion status of the second phase is extremely important in order to acquire a material with cluster-level structure. Moreover, a starting powder with the condition of fine, homogeneous microstructure and without secondary particles is required for the highly functional ceramics [8]. Therefore, an alternative process, coprecipitation process, was adopted in the present work to obtain a correct level of dispersion of the dopant and a required grain size of the Al_2O_3 matrix. Some advantages of the coprecipitation method are better homogeneity, high purity and lower sintering temperature, which were thought to be suitable for producing molecular-level solid-solutions [9].

In this chapter, the homogeneously dispersed powder mixture of Al_2O_3 and 1.0 mol% Cr_2O_3 was prepared by using the coprecipitation process at various calcination temperatures. X-ray diffraction, scanning and transmission electron microscopy was applied to determine the microstructure of the powders.

4.2 Experimental

Reagent-grade hydrous aluminum nitrate [$Al(NO_3)_3 \cdot 9H_2O$, purity 99%] and chromium nitrate [$Cr(NO_3)_3 \cdot 9H_2O$, purity 99.9%] were used as the starting materials for the coprecipitation process. The aluminum and chromium nitrates with concentration of 0.5 mol/l were prepared by dissolving them in distilled water. The aqueous solution with 1 mol% $Cr(NO_3)_3$ was mixed in a magnetic stirrer for two hours at room temperature. Subsequently, the solution was carefully added to the aqueous ammonia (NH_4OH, 0.5M)
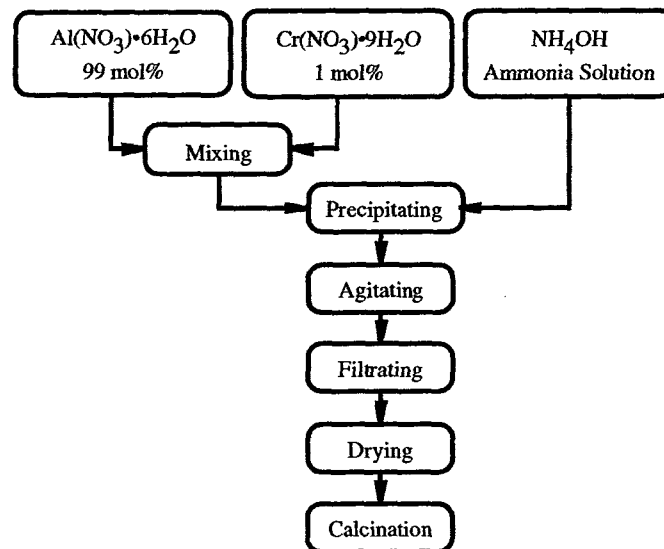
Fig. 4-1 Schematic illustration of coprecipitation procedure.

during continuous stirring until the pH value reached level of 10. The suspension was filtered and washed with distilled water for five times to remove absorbed water and nitrate ions. Further, the remainder was dried in a constant temperature at 60°C.

Differential thermal and thermogravimetric analyze (DTA/TG) of the obtained powder was performed in air with a heating rate of 10°C/min. The α-alumina was used as the standard reference material for DTA/TG examination. The obtained powder was also investigated by *in-situ* high temperature X-ray diffractometry (HT-XRD, Scintag Inc.) using a Pt heater which can allow us to heat the sample upto the temperature of 1500°C. In order to avoid the complexity of the phase composition of the Al_2O_3 powders, the calcination temperatures were selected to equal 1000°C, 1100°C and 1200°C, following our belief that the existing alumina is transformed completely into α-Al_2O_3 at these particular temperatures,. The size of the particles of the calcinated powder was investigated by centrifugal particle size analyzer (SA-CP3L, Shimazu Industry Co.). The microstructure was examined prior and after the treatment by the transmission electron microscopy (TEM).

4.3 Results and Discussion

Thermal analysis of the obtained powder revealed a distinct endothermic peak at approximately 100°C, being accompanied by a concurrent weight loss due to evaporation of the absorbed water (see Fig. 4-1a). Another small endothermic peak was observed at 250°C. Based on the high temperature X-ray measurements, we conclude that this peak appearance is caused by dehydration of the obtained powder – mainly bayerite ($Al_2O_3 \cdot H_2O$). The exothermic peaks for chromia precursor were not observed during present experiments, due to the low amount of the chromium nitrate. In the case of Cr_2O_3 monolith prepared by same ocedure, one endothermic peak and two exothermic peaks were observed (Fig. 4-2b). The first endothermic peak at about 100°C can be ascribed to the loss of the adsorbed water. The first exothermic peak at about 250°C maybe due to the oxidation of NO_3. The crystallization of chromia was depicted as the second exothermic peak at 400°C, which agree to the XRD results.

The XRD examination was performed for pure Al_2O_3, Cr_2O_3 and Al_2O_3 doped with 1.0 mol% Cr_2O_3 (Fig. 4-3). It was found that at room temperature the obtained alumina powders contain mainly bayerite ($Al_2O_3 \cdot H_2O$), while at 250°C the transformation to η-alumina starts in a consequence of dehydration. The peaks of η-alumina are found for the temperatures higher than 500°C. The θ- and α- Al_2O_3 peaks was registered at the temperatures at 900°C
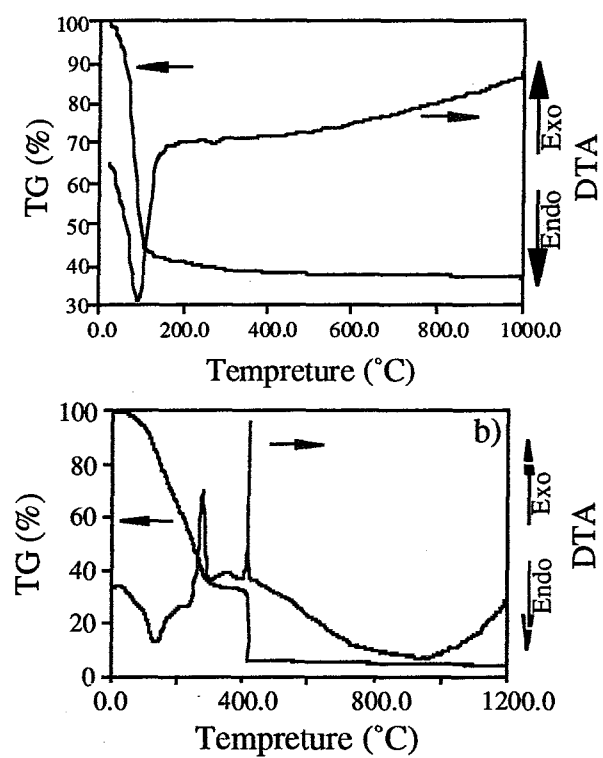
Fig. 4-2 TG/DTA results of Al_2O_3-1.0 mol% Cr_2O_3 powders (a) as well as Cr_2O_3 (b) prepared by coprecipitation process.
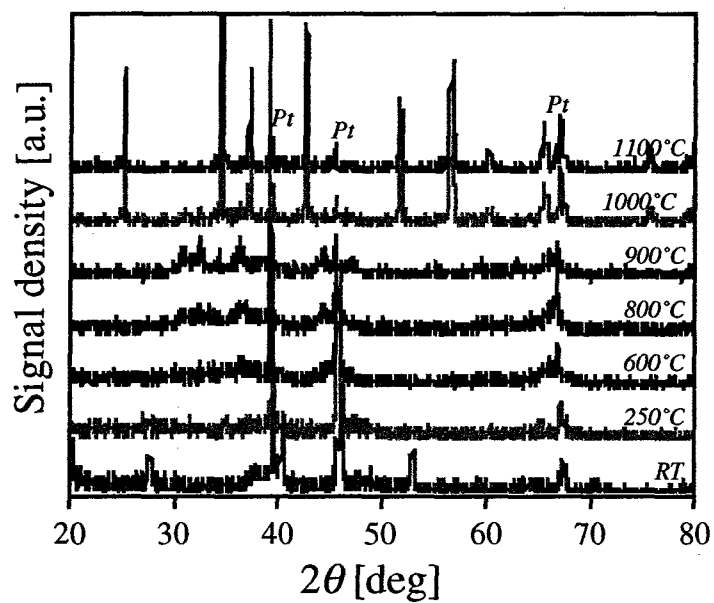

Fig. 4-3 In-situ high temperature XRD patterns of Al_2O_3-1.0 mol% Cr_2O_3 powders prepared by coprecipitation process.

and 1100°C, respectively. The peak of crystalline Cr_2O_3 was observed at 450°C, while we found no difference in the spectra obtained for the coprecipitated suspension of Cr_2O_3 with increasing temperature. In the case of the 1.0 mol% Cr_2O_3 doped Al_2O_3, the phase transformation occurred earlier in higher temperatures than that being characteristic for crystallization of Cr_2O_3, because the homogeneously dispersed Cr_2O_3 stabilizes Al_2O_3 structure. This gives us a chance to obtain finer grain α-Al_2O_3 powder than Al_2O_3 monolith by using lower calcination temperature. The phases appeared during the calcination procedure and detected by means of in-situ high temperature X-ray diffraction are listed in Fig. 4-4.

Taking into account the results of X-ray examination, the selection of the calcination temperatures has been made, and the dried powder was treated at 1000°C, 1100°C and 1200°C for 2 hours with the heating rate of 10°C/min to avoid the complex phase changes during the sintering process. However, the X-ray patterns showed that the powder is a mixture of θ- and α-phase for the calcination temperature of 1100°C. It is caused by the heterogeneous heating which is believed to occur when a large volume of the powder is calcinated (see Fig. 4-5).

TEM observation shows the particle size of the powder changes significantly with calcination temperature (see Fig. 4-6). The powder calcinated at 1000°C possess a particle size of about 20nm (Fig. 4-6a). However, the large second particles were also observed because of the particle aggregation of θ-Al_2O_3 particles. On the other hand, the powder consists of mono-dispersed particles showing uniform faceted morphology (200nm in size) after calcinated at 1200°C (Fig. 4-6b).

The particle size distributions of the calcinated powder investigated centrifugal particle analysis are shown in Fig. 4-7. For the low calcination temperature, the powder possessed a smaller particle but wide distribution because of the agglomeration of θ-alumina, which agreed the TEM observations. The powder calcinated at 1200°C exhibited narrow size distribution, since all the particles were transformed to α-Al_2O_3. On the viewpoint of sintering process, the powder in the shape of fine, homogeneous and without secondary particles is preferred to obtain better properties of ceramics. Therefore, we can conclude that the powder calcined at 1200°C should have a better sintering ability.

The micrograph of high resolution TEM observation is depicted in Fig. 4-8. The arrows shows the dislocation of crystalline occurred inside Al_2O_3 matrix. It should be emphasized that these dislocations were in size of less than 1 nm. This dislocation can be deduced from AlO_6^{-6} cluster replaced by larger CrO_6^{-6} cluster.

Fig. 4-4 Different phases of coprecipitation delivered Al_2O_3 and Cr_2O_3 observed by in-situ high temperature X-ray diffraction.
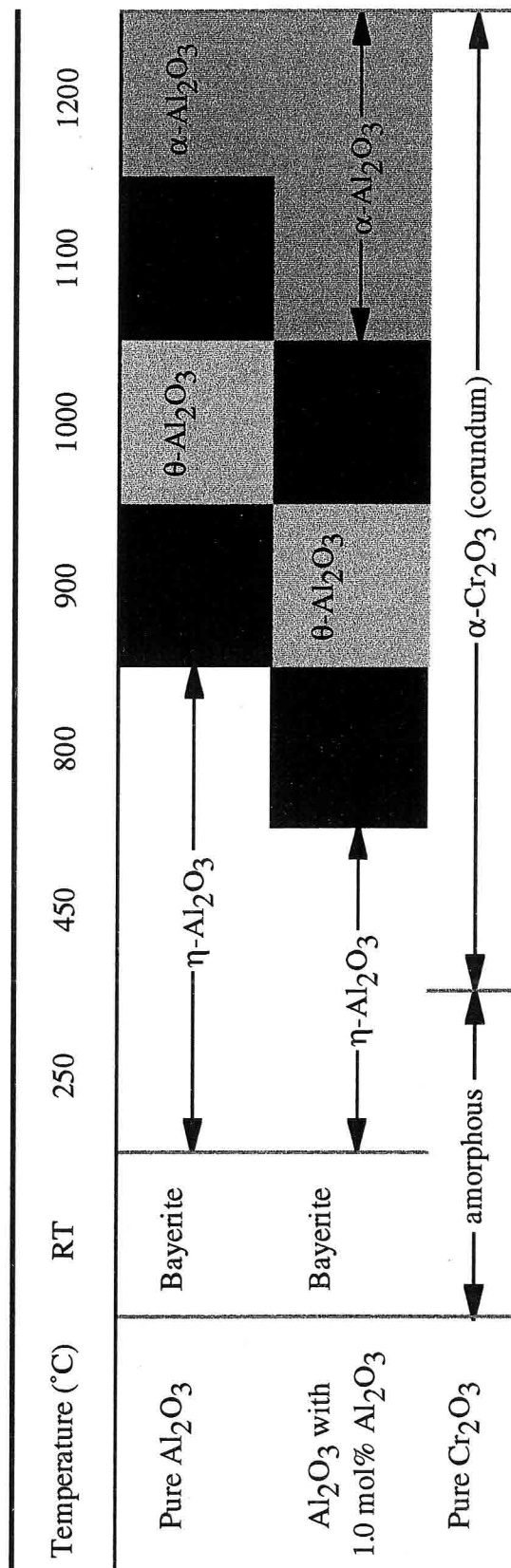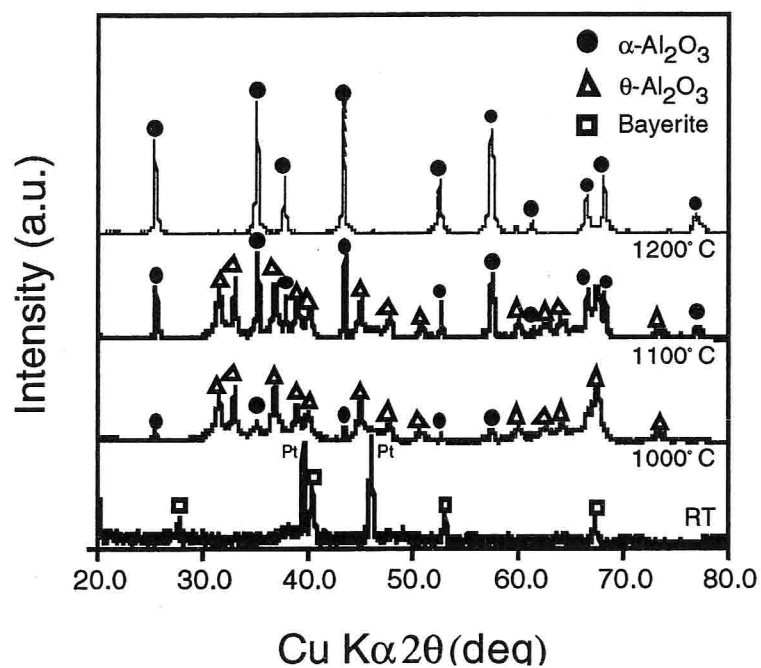
Fig. 4-5 X-ray diffraction patterns of coprecipitated Al_2O_3-Cr_2O_3 powders after calcination.
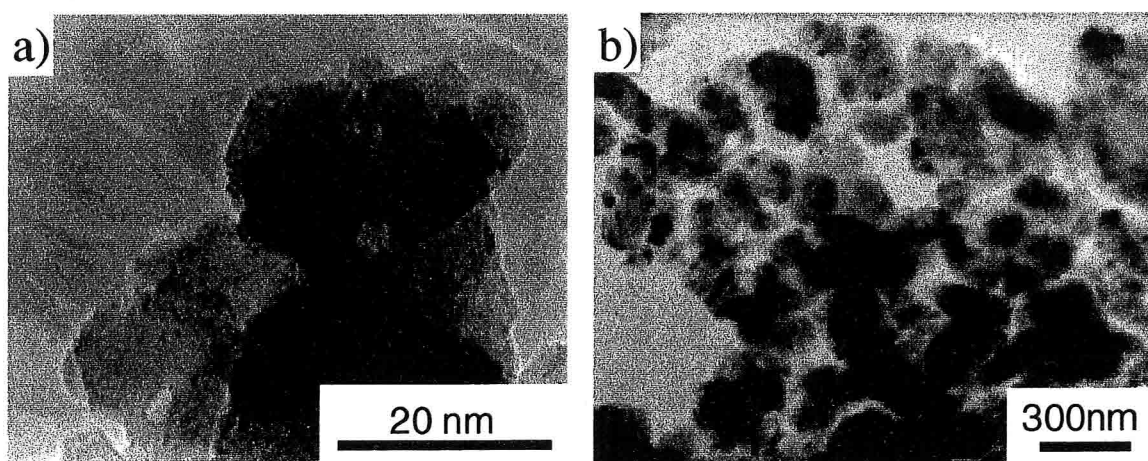

Fig. 4-6 TEM micrographs of the mixed powders calcinated at 1000°C (a) and 1200°C (b).

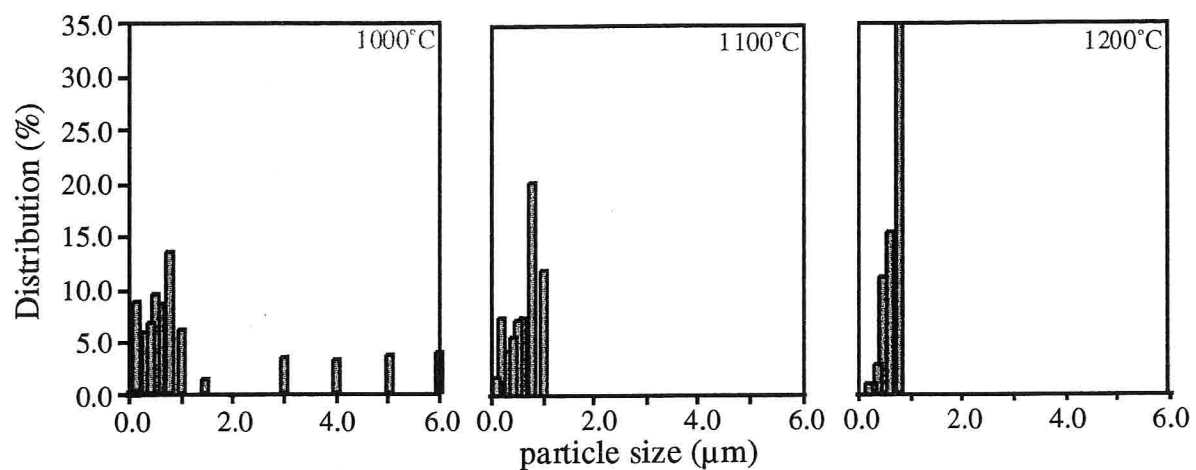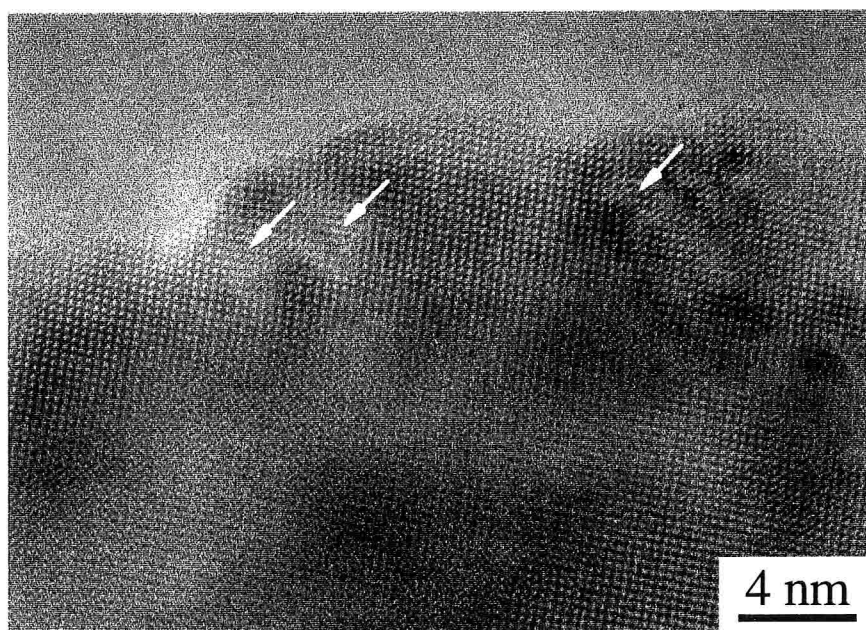Fig. 4-7 Particle size distribution of the Al_2O_3-1.0 mol% Cr_2O_3 mixing powder after calcination

Fig. 4-8 HREM micrographs of Al_2O_3-1.0 mol% Cr_2O_3 powders obtained after calcinated at 1200°C.

4.4 Conclusions

The coprecipitation process proved to be efficient for obtaining the homogeneous and fine structure of Al_2O_3-1.0 mol% Cr_2O_3 powder mixture. It was found that the particle-size and the phase-content could be controlled by the selection of the calcination temperature. The powder calcinated at 1200°C possessed exclusively α-Al_2O_3 phase and exhibited the limited distribution of particle-size. HREM observation comfirmed that the Cr_2O_3 was dispersed in the cluster-level within the inside of Al_2O_3 matrix grains.

References

1   H.P. Kirchner and R.M. Gruver, J. Am. Ceram. Soc., 49, 330 (1966)

2   H.P. Kirchner , R.M. Gruver and R.E. Walker, J. Am. Ceram. Soc., 50, 169 (1967)

3   H.P. Kirchner , R.M. Gruver and R.E. Walker, J. Am. Ceram. Soc., 51, 250 (1968)

4   P.H. Giltzen, in: Alumina as a ceramic Material, American Ceramic Society, Columbus, OH, 1970

5   W.D. Kingery, H.K. Bowen, DR. Uhlmann, in: Introduction to Cereamics, John Wiley & Sons Inc., 1976, pp. 131-139

6   E.N. Bunting, J. Res. Nat. Bur. Stand., 6, 947-949 (1931)

7   C.L. Li, D.-H. Riu, T. Sekino and K. Niihara, Key Engineering Materials, 161-163, 161 (1999)

8   S. Satuka, in: The science of sol-gel process, Agune Shofu Ltd., 1988, pp. 104-114

9   Y. Ozaki, Ceramics, 21, 102-110 (1986)

10 D.-H. Riu, C.L. Li, H.-E. Kim and K. Niihara, Key Engineering Materials, 161-163, 521 (1999)

7   K. Niihara, J. Ceram. Soc. Jpn., 99, 974 (1991)

9   P.D. Ownby and O.P. Lahmann, Powder Met. Int., 7, 172 (1975)

10 H.G. Emblem, T.J. Davies, A. Harabi, A.A. Ogwu, C.S. Nwobodo and V.Tsantzalou, J. Mater. Sci. Lett., 11, 820 (1992)

11 N. Murayama, Ceramics, 32, 115 (1997)

12 Kawabata, M. Yoshinaka, K. Hirota and O. Yamaguchi, J. Am. Ceram. Soc., 78, 2271 (1995)

Chapter 5

Fabrication and Characterization of Al_2O_3-Cr_2O_3 solid solution by Pulse Electric Current Sintering

The Al_2O_3-1.0 mol% Cr_2O_3 was fabricated by Pulse Electric Current Sintering (PECS) method using the homogeneously dispersed mixture obtained in previous chapter. The cluster-level microstructure of sintered body was observed by TEM, which was proved by CBED patterns. This cluster-level structure was generated through the matrix AlO_6^{-6} cluster replaced by CrO_6^{-6} cluster. The specimen sintered from the powder calcinated at 1200°C exhibited considerably higher mechanical properties than the sample obtained by the conventional powder mixing.

5.1 Introduction

Much attentions have been paid on nanocomposite - a new concept of materials proposed by Niihara which significantly increase the mechanical properties of the ceramics [1-11]. It was known that nanocomposites can not only modify the mechanical properties but also give the ceramics new functions depended on the properties of the dispersions [12-13]. Therefore, we can predict that a molecular/cluster level composite can also give the composite a complete new functions without decrease of the mechanical properties.

In chapter 3, the improvement of the mechanical properties of the Al_2O_3-Cr_2O_3 solid solution with a low amount of Cr_2O_3 - which was prepared by powder mixture process - was already discussed. It was found that the dispersion of Cr_2O_3 could significantly affect the properties of the sintered material. Consequently, a coprecipitation process has been adopted to obtain a cluster level of dispersion of the dopant and a fine grain size of mixing powder, which has be described in previous chapter.

5.1.1 Pulse Electric Current Sintering

Pulse electric current sintering (PECS) is a newly developed process – a synthesis and processing technique – which makes possible sintering and sinter-bonding at low temperatures and short periods by charging the intervals between powder particles with electrical energy and effectively applying a high electric current pulse [14]. It exploit self-heating action from inside of the powder, similar to self propagating high-temperature synthesis (SHS) and microwave sintering. PECS method offers many advantages such like

high sintering speed, increasing surface activation of particles, high-speed diffusion/material transfer and short sintering time compared with over conventional sintering method. The schematic illustration has been depicted in Fig. 5-1.

5.1.2 Convergent Beam Electron Diffraction (CBED)

Convergent beam electron diffraction is an alternative method of decreasing the size of the area giving rise to the diffraction pattern to illuminate only a very small area by focusing the electron source onto the specimen [15]. The schematic diagram has been depicted in Fig. 5-2b compared with general selected area diffraction (SAD, Fig. 5-2a). The relation of zero order laue zone (ZOLZ) and high order laue zone (HOLZ) has been shown in Fig. 5-3a. When we take the ZOLZ pattern on the HOLZ plane, the diffraction disk can be obtained as illustrated in Fig. 5-3b. HOLZ line can be observed clearly inside this ZOLZ disc, which is caused by the HOLZ reflection satisfied the Bragg's condition. The position of HOLZ lines is extremly amenable to the change of lattice constant and the wavelength of the electron ray. On the otherhand, the HOLZ line can be used to measure the lattice constant and lattice distortion of localized area, and the accuracy can be reached to 0.1%.

In this chapter, the mechanical properties and microstructure of Al_2O_3-Cr_2O_3 solid solution sintered by PECS process were addressed. X-ray diffraction, scanning and transmission electron microscopy were applied to determine the microstructure of sintered compacts. We has specially used the convergent beam electron diffraction (CBED) to verify the cluster-level microstructure.

5.2 Experimental

The Al_2O_3-Cr_2O_3 solid solution was produced in a graphite mold by using pulsed electric current sintering method (PECS) with a heating rate of 100°C/min. The sintering was carried out at 1400°C for 5 minutes, in argon atmosphere under the applied pressure of 30 MPa.

We prepared the test bars size of 2×3×25 mm of sintered compact which surface was grounded and polished with tensile beveled edges to avoid the formation of edge cracks. The density of the product was measured by Archimedes' immersion method in toluene, while Young's modulus was determined by using the supersonic resonance method.

The three-point bending test (span of 20 mm) was performed with a crosshead speed of 0.5 mm/min and the load applied in parallel to the sintered axis. In order to determine the fracture strength, at least five independent measurements were made for each specimen. The
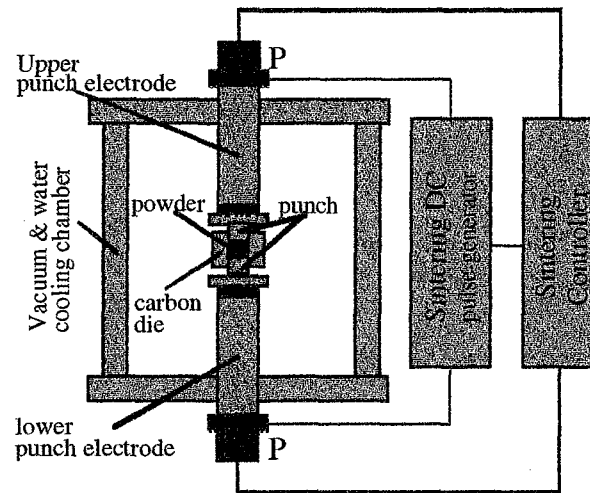
Fig. 5-1 Schematic illustration of pulse electric current sintering system
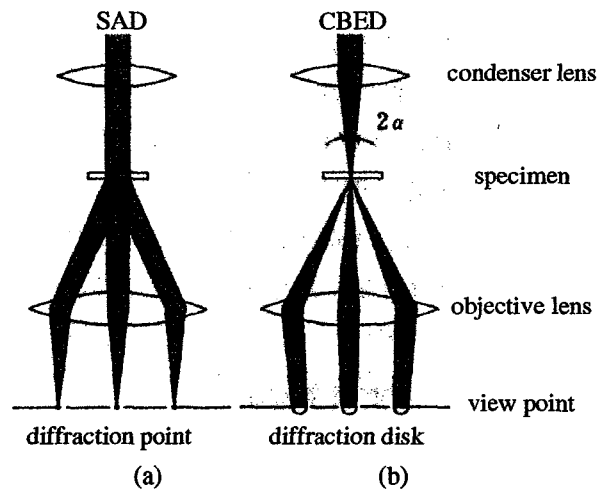

Fig. 5-2 Schematic diagram for general selected area diffraction (a) and convengent beam eletron diffraction (b).
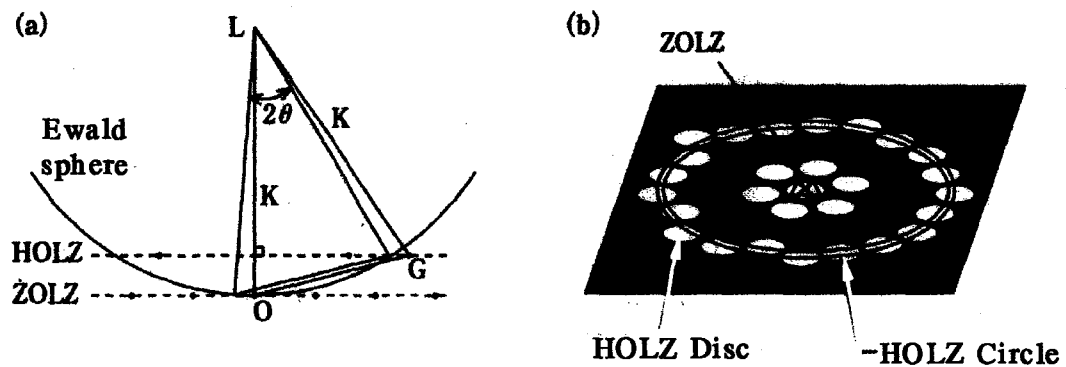

Fig. 5-3 Schematic diagram of relation of HOLZ and ZOLZ (a) and CBED image (b).

microscopic and fractographic observations of the prepared Al_2O_3-Cr_2O_3 samples were performed by means of scanning electron microscopy (SEM). TEM and CBED obervations were also carried out to validate the obtained microstructure.

5.3 Results and Discussion

5.3.1 Microstructure

The observed HRTEM images of the Al_2O_3 + 1.0 wt% Cr_2O_3 solid solution specimens has been shown in Fig. 5-4. Although it looks like an image of typical Al_2O_3 microstructure, some inhomogenity of the structure in the nano-size areas can be observed with different view contrast. This may be caused by the cluster-level distribution of the bigger CrO_6^{-6} cluster causing the electron scatting in the solid solution structure.

To confirm this interpretation some convergent beam electron diffraction studies has been carried out on the white and black areas. The results were shown in Fig. 5-5. The perfect structure of Al_2O_3 represent a clear HOLZ pattern (Fig. 5-5a). In contrast, the point-out arrows show the widening of the HOLZ lines for the dark area of structure (see Fig. 5-4). This results proved that the lattice constants of Al_2O_3 have been modified because of the bigger CrO_6^{-6} cluster distribution. Therefore, we can conclude that the cluster-level composite has been successfully fabricated through using homogeneously coprecipitated Al_2O_3-Cr_2O_3 mixed powder and PECS sintering process.

SEM observations of the morphology of matrix grains were carried out to examine the microstructure of Al_2O_3-Cr_2O_3 solid solution sintered by PECS process (Fig. 5-6). The variations in grain size were observed for the specimens prepared at different calcination temperatures. The dominant decrease in grain size was found for the material calcinated at 1200°C in contrast to the other specimens (compare with Figs. 5-6a, 5-6b and 5-6c). The sintered samples of low temperature calcinated powder posses larger grains (see Fig. 5-6d), which may be attributed to the existence of the θ- Al_2O_3 particles in the dried powder. However, using the homogenous powder prepared by the coprecipitation, we may reduce the grain size to less than 1 μm. The microstructure of monolith Al_2O_3 and Al_2O_3-Cr_2O_3 solid solution from the conventional powder mixture sintered under similar conditions, is shown in Fig. 5-6e and 5-6f, respectively. One can notice that the grain size in Fig. 5-6d is considerably larger than that of the structure shown in Fig. 5c. It can be concluded that the cluster-level homogeneous dispersed CrO_6^{-6} play an important role in inhibiting the grain growth during the sintering process.
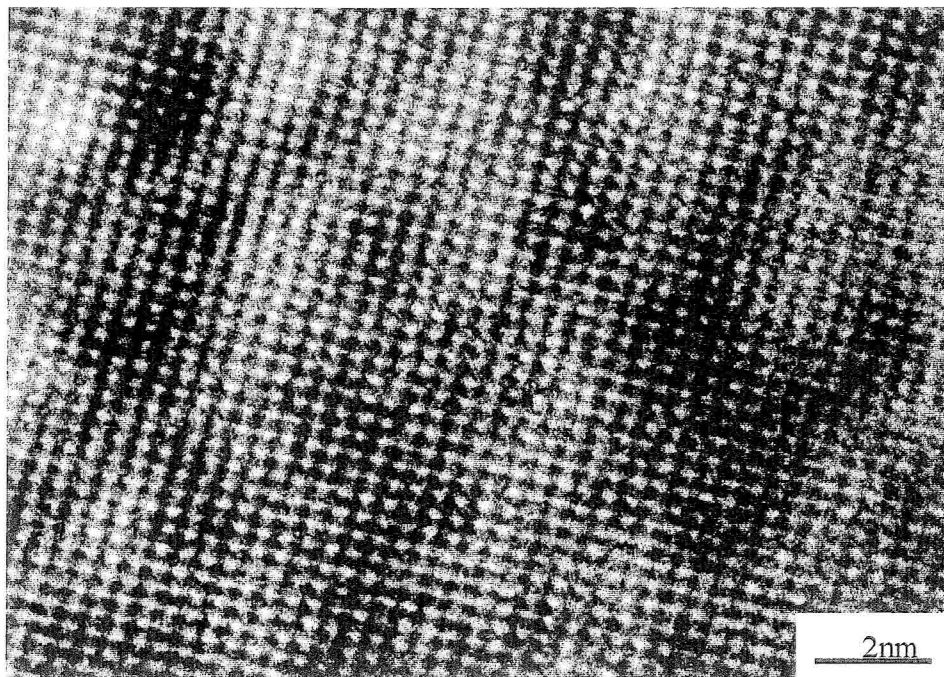
Fig. 5-4 HREM image of Al$_2$O$_3$+1.0 mol% Cr$_2$O$_3$ specimen obtained from using the powder calcinated at 1200°C.

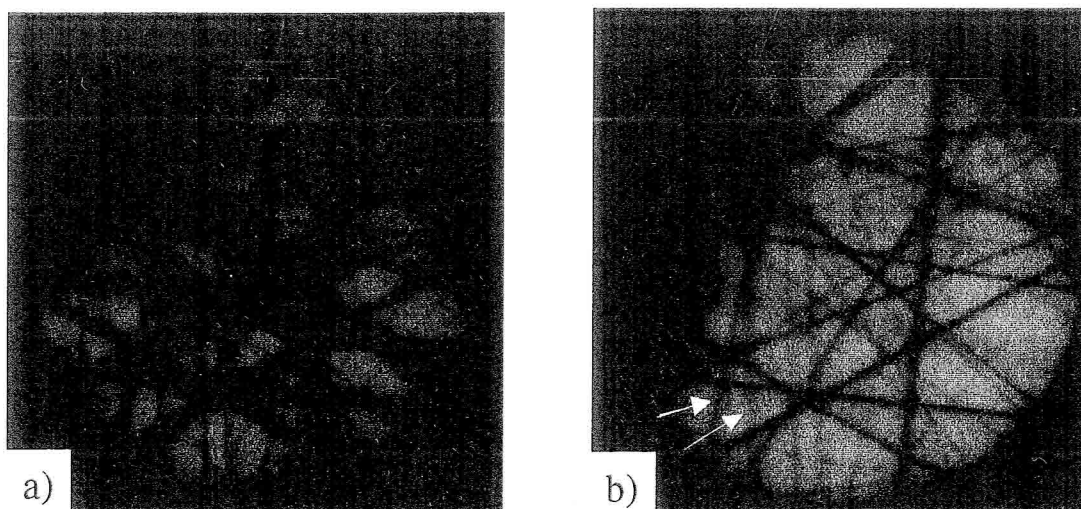

Fig. 5-5 HOLZ pattern for Al$_2$O$_3$+1.0 mol% Cr$_2$O$_3$ specimen obtained from perfect structure (a) and from non-homogeneous area (b); the lines indicated by narrows show changes in lattice parameters.
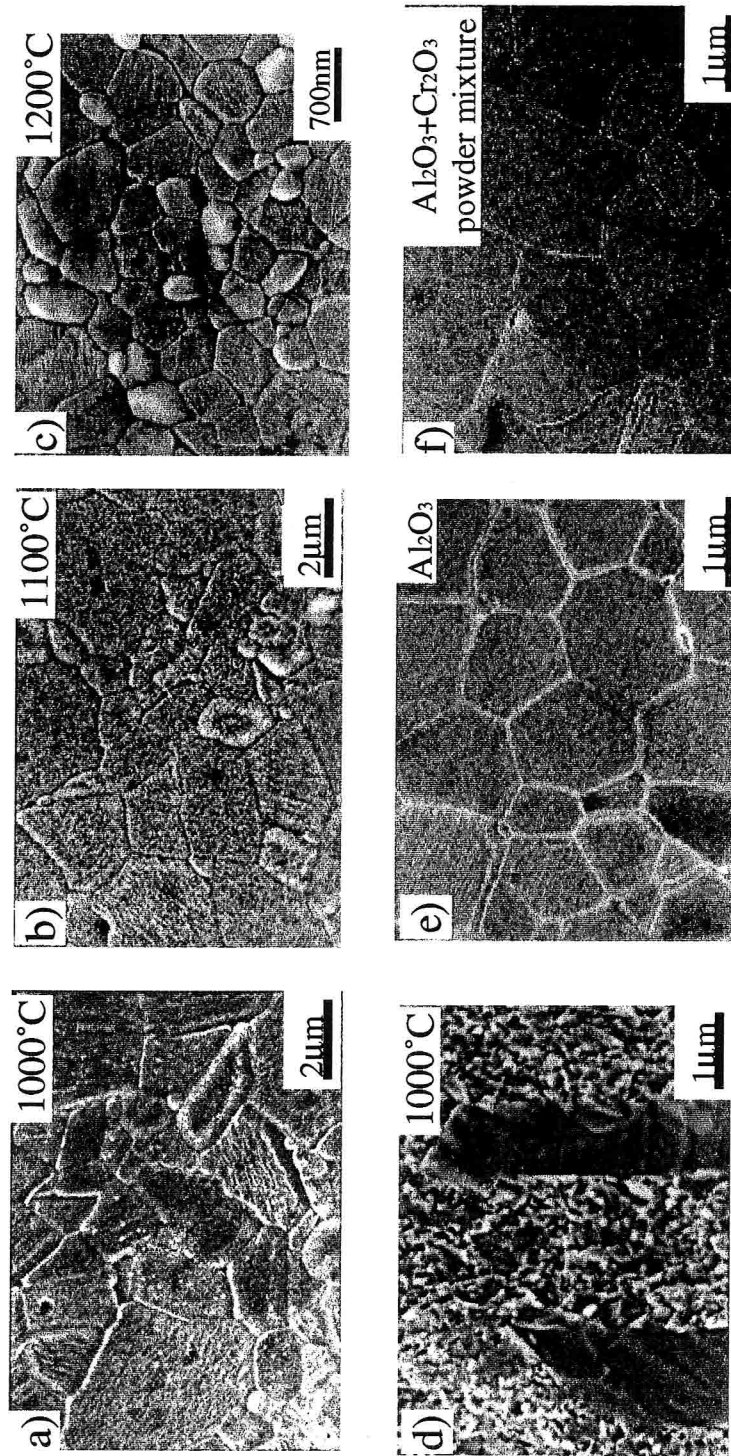
Fig. 5-6 SEM micrographs of etched surface microstructure of materials sintered by PECS for a different calcination temperature.

70

5.3.2 Mechanical Properties

The mechanical properties of Al_2O_3-Cr_2O_3 solid solution sintered by PECS process are summarized in Table 5-1 and compared with the results for pure alumina prepared by the same process. Those obtained for the powder mixture produced by conventional method are also listed. The relative density of the specimens exceeded 99% except the sample of pure Al_2O_3 calcinated at 1200°C. The Al_2O_3-Cr_2O_3 solid solution calcinated at 1200°C showed the highest density, since the fine homogeneous starting powder had completely transform to α-Al_2O_3 phase, posses a good sintering ability.

The sintered Al_2O_3-Cr_2O_3 solid solution using the powder calcinated at 1000°C shows a extremly low value of fracture strength because the strange grain growth of the aggregation of θ-Al_2O_3 in the calcinated powder during the sintering process. For the sintered samples calcinated at lower temperatures, the strength are dependent on the amount of the θ-Al_2O_3 which remained after calcination. The above-mentioned phenomenon is also responsible for the above discussed increase in grain size (Fig. 5-6). The sintered Al_2O_3-Cr_2O_3 solid solution using the powder calcinated at 1200°C, which posses a smallest grains (refer to SEM micrograph - Fig. 5c), exhibited the high fracture strength. The described effect is associated with the residual stress caused by the Cr_2O_3 cluster dispersed in Al_2O_3 matrix. It is worthy to emphasize that the strength of sintered Al_2O_3-Cr_2O_3 solid solution using the powder calcinated at 1200°C prepared by coprecipitation technique was twice as high as that measured for the conventionally mixed powder. Because of possessing the cluster-level controlled microstructure, all of the mechanical properties of this material show much more improved mechanical properties than all other materials.

Table 5-1 Mechanical properties of materials prepared by PECS sintering process

Specimen	Al_2O_3-Cr_2O_3			Al_2O_3			Al_2O_3-Cr_2O_3 powder mixture
	1000°C	1100°C	1200°C	1000°C	1100°C	1200°C	
Relative density (%)	99.45	99.29	99.87	99.88	99.46	94.71	99.09
Yong's modulus (GPa)	394.8	393.2	398.7	398.5	395.1	340.4	392.1
Fracture strength (MPa)	241±41	722±80	855±41	460±46	596±96	433±25	408±96
Hardness (GPa)	15.1	15.3	17.4	13.8	15.6	13.5	14.8
Fracture toughness $(MPa \cdot m^{1/2})$	3.46	3.23	3.35	2.79	2.76	3.19	3.09

5.4 Conclusions

The sintered Al_2O_3 and 1.0 mol% Cr_2O_3 solid solution have been fabricated by using PECS method. The cluster-level composite of Al_2O_3-Cr_2O_3 has been successful achieved, which has been recognized by high resolution TEM observation and CBED studies. Due to the novel microstructure, the grain size have been successfully suppressed, while better mechanical properties has been obtained than the specimens sintered from monolithic Al_2O_3 and conventional mixed powder. The strength of obtained materials was twice as high as that obtained for samples produced by conventional powder mixture method. This study has revealed that cluster-level composite could significantly increase the mechanical properties of the matrix material.

Conclude for chapter 4 & 5, this study provides a successful way leading to the preparation of homogeneously cluster-level dispersed Al_2O_3-Cr_2O_3 solid solution by using coprecipitation technique to obtain fine homogeneous cluster-level dispersed mixture, and by fast PECS sintering to achieve cluster-level composite.

References

1   K. Niihara, J. Ceram. Soc. Jpn., **99**, 974 (1991)

2   K. Niihara, A. Nakahara, T. Uchiyama and T. Hirano, in Fracture Mechanics of Ceramics, 7, Eds. by R.C. Bradt, A.G. Evans, D.P.H. Hasselman and F.F. Lange, Plenum Press, 1986, pp. 103-116

3   A. Nakahara and K. Niihara, in Fracture Mechanics of Ceramics, 7, Eds. by M. Sasaki, R.C. Bradt, D.P.H. Hasselman and D. Munz, Plenum Press, 1992, pp. 165-178

4   T. Ohji, A. Nakahira, T. Hirano and K. Niihara, J. Am. Ceram. Soc., 77, 3259-3262 (1994)

5   E. Yasuda, Q.Bao and K. Niihara, J. Ceram. Soc. Jpn., 100, 514-519 (1992)

6   G. Sasaki, H. Nakase, K. Suganuma, T. Fujita and K. Niihara, J. Ceram. Soc. Jpn., 100, 536-540 (1992)

7   T. Sekino, A. Nakahira, M. Nawa and K. Niihara, J. Jpn. Soc. Powder Powder Metall., 38, 326-330 (1991)

8   M. Nawa, T. Sekino and K. Niihara, J. Mater. Sci., 29, 3185-3192 (1995)

9   T. Sekino and K. Niihara, Nanostruct. Mater., 6, 663-666 (1995)

10 M. Nawa, K. Yamazaki, T. Sekino and K. Niihara, J. Mater. Sci., 31, 2848-2858

11 A. Nakahira, H. Tamada and K. Niihara, J. Jpn. Powder Powder Metall., 41, 514-517 (1994)

12 K. Niihara, Y.-H. Choa, M. Hussain, Y. Hamahashi, H. Kawahara, Y. Okamato and H. Nishida, Materials Integration, 12 (5), 47-53 (1999)

13 K. Niihara, T. Kusunose, S. Kohsaka, T. Sekino and Y.-H. Choa, Key Engineering Materials, 161-163, 527-534 (1999)

14 M. Tokita, J. Soc. Powder. Tech. Jpn., 30, 790-804 (1993)

15   G. Thoma and M.J. Goringe, in: Transmission Electron Microscopy of Materials, John Wiley & Sons Inc., 1979, pp.45-138

Chapter 6

Summary and Conclusions

In this study, the author proposed to develop a completely new type of ceramics with microstructure controlled by molecular/cluster-level dispersiods – molecular/cluster-level composite. Attention was focused on the mixing process, powder, sintering method, temperature, volume and other relevant conditions for the fabrication and characterization cluster-level composites. The effects of molecular/cluster dispersiods on the crystal microstructure and mechanical properties prepared by ion bombardment have also been evaluated by nano-indentation method. General powder metallurgical method has been adopted to prepare Al_2O_3-Cr_2O_3 nanocomposites with inclined interface on the grain boundary. Coprecipitation method was selected to obtain the homogeneously dispersed Al_2O_3-Cr_2O_3 mixture on the cluster level. Further, the cluster-level composite was achieved by using the new PECS process. The main conclusions in this study are summarized as follows.

In chapter 2, the difference on deformation behavior of the virgin and modified sapphire was studied in order to verify the influence of the cluster-level dispersiods on the crystal structure control. The second phase was introduced into matrix sapphire on the cluster-level by suing ion implantation method. The unimplanted Al_2O_3 is characterized by a sharp pop-in of plastic deformation at contact stress well in excess of the steady-state hardness of the material. The twinning structure occurred on the (1010) plane of the sapphire showed a regular saw-like structure, which was observed on the first time using the atomic force microscopy. The cluster-level dispersed second phases give the matrix crystal a smooth transition from elastic to plastic behavior. This difference in mechanical properties is associated with the presence of cluster-size dispersiods able to move at a critical shear stress whereas for the virgin material the paucity of such dislocations requires a significant overload to initiate such deformation.

All the above results show that the cluster-size dispersiods would make a critical effect on the structure and mechanical properties of the matrix material. It means that we can modify the fracture manner like twinning and cracking by cluster-level composite technique, which is quite important for applications in the ceramic materials in industry.

In chapter 3, high content of Cr_2O_3 addition shows the possibility of microstructure control through inhibiting the grain size development during the sintering process. However, we can not find any effect caused by nano/cluster-level composition on Al_2O_3-Cr_2O_3 solid solutions with the high content of Cr_2O_3 addition.

In the case of low content of Cr_2O_3 addition, we found that the lattice parameter of our material increased for the Cr_2O_3 content exceeding 0.6 mol%. Further, we found the increase in grain size when Cr_2O_3 is located inside the Al_2O_3 matrix grains. The maximum strength of the material was achieved for Al_2O_3 containing 0.4 mol% of Cr_2O_3. The nano-indentation results proved that the small addition of chromia can affect the mechanical properties of alumina. Hardness of Al_2O_3-Cr_2O_3 solid solution was higher when the content of Cr_2O_3 exceeds 0.7 mol%. Microstructure observations show that low addition of Cr_2O_3 can affect the matrix structure on the level of the nano-size, with an incline distribution on the grain boundary. The large particle size of starting powder is the main barrier on fabricating the cluster-level composite which caused the inhomogeneous solid solution inside matrix.

In chapter 4, the coprecipitation process proved to be efficient in obtaining the homogeneous and fine structure of Al_2O_3-1.0 mol% Cr_2O_3 powder mixture. It was found that the particle-size and the phase-content could be controlled by the selection of the calcination temperature. The powder calcinated at 1200°C possessed exclusively α-Al_2O_3 phase and exhibited the limited distribution of particle-size. HREM observation comfirmed that the Cr_2O_3 which was dispersed on the cluster-level inside Al_2O_3 matrix.

In chapter 5, the sintered Al_2O_3 and 1.0 mol% Cr_2O_3 solid solution has been fabricated by using PECS method. The cluster-level composite of Al_2O_3-Cr_2O_3 has been successfully achieved, which has been recognized by high resolution TEM observation and CBED studies. Due to the novel microstructure, the grain size has been successfully suppressed, while better mechanical properties has been obtained than the specimens sintered from monolithic alumina and conventional mixed powder. The strength of obtained materials was twice as high as that obtained for samples produced by conventional powder mixture method. This study has showed that cluster-level composite can significantly increased the mechanical properties of the matrix material.

As a whole, a novel material design concept for Al_2O_3, controlling the material matrix on the molecular/cluster level, was attempted by the present author by using various powder

75

making and sintering process. This study provides a successful way leading to the preparation of homogeneously cluster-level dispersed Al_2O_3 based ceramics. Compared with microcomposites and nanocomposites technique, this new generation of material design, molecular/cluster level composite, is expect to contribute their application on all of ceramics especially in the electronics ceramics.

List of Publications

Papers

1   C.L. LI, D.-H. RIU, T. SEKINO and K. NIIHARA,
    Fabrication and Mechanical Properties of Al_2O_3 Solid Solution with Low Addition of Cr_2O_3,
    Key Engineering Materials, 161-163, 161-164 (1999)

2   D.-H. RIU, C.L. LI, H.-E. KIM and K. NIIHARA,
    Novel Microstructural Design of Alumina Based Ceramics,
    Key Engineering Materials, 161-163, 521-526 (1999)

3   R. NOWAK, C.L. LI and M. V. SWAIN,
    Comparison of Implantation with Ni^{2+} and Au^{2+} Ions on the Indentation Response of Sapphire,
    Materials Science and Engineering, A253, 167-177 (1998)

4   C.L. LI, D.-H. RIU, T. SEKINO and K. NIIHARA,
    Preparation and Mechanical Properties of Al_2O_3-Cr_2O_3 Solid Solutions,
    Journal of European Ceramics Society, (in contribution)

5   C.L. LI, T. SEKINO, Y.-H. Choa and K. NIIHARA
    Characterization of Al_2O_3-Cr_2O_3 Solid Solution Prepared by Coprecipitation Technique,
    Materials Letters, (in contribution)

6   C.L. LI, R. NOWAK, T. SEKINO and K. NIIHARA,
    Surface Deformation of the $(1\bar{2}10)$ Plane of Sapphire, (in preparation)

Proceeding

7   C.L. LI, D.-H. RIU, T. SEKINO and K. NIIHARA,
    Characterization of Al_2O_3-Cr_2O_3 Solid Solution Prepared by Coprecipitation Technique,
    Proceeding of the 3rd International Nano Ceramic Forum and the 2nd International Symposium on Intermaterials, 52-57, (June 9-12, 1999, Seoul, Korea)

8   D.-H. RIU, Y.-H. CHOA, C.L. LI H.-E. Kim and K. NIIHARA,
    Fabrication of Alumina-Chromia Solid Solution with Core-shell Structure and Related Mechanical Properties,
    The 3rd International Meeting of Pacific Rim Ceramics, 142, (September 20-23, 1998, Kyongju, Korea)

List of Supplementary Publications

9   Y. WATANABE, S. UCHIYAMA, Y. NAKAMURA, C.L. LI, T. SEKINO and K. NIIHARA,
    Mechanical Properties and Residual Stress in AlN/Al Mixed Films Prepared by Ion-beam-assisted Deposition,
    Journal of Vacuum Science and Technology, A17 (2), 603-607 (1999)

10 R. NOWAK, C.L. LI, T. OKADA and F. YOSHIDA,
    Nano-Indentation of Ion-beam Modified HfN/Si System: Identification of the Amorphized Inter-layer,
    Nuclear Instruments and Methods In Physics Research, B148, 110-115 (1999)

11 R.R. MANORY, C.L. LI, C. FOUNTZOULAS, J.D. DEMAREE, J.K. HIROVONEN and R. NOWAK,
Effect of Nitrogen Ion-Implantation on the Tribological Properties and Hardness of TiN Films,
Materials Science and Engineering, A253, 319-327 (1998)

12 R. NOWAK, Y. MIYAGAWA, C.L. LI, S. NAKAO, S. MARUNO and S. MIYAGAWA,
Post-deposition Reduction of Internal Stress in Thin Films: The Case of HfN Coating Bombarded with Au Ions,
Materials Letters, 33, 31-36 (1997)

13 R. NOWAK, C.L. LI and S. MARUNO,
Low-load Indentation Behavior of HfN Thin Films Deposited by Reactive rf Sputtering,
Journal of Material Research, 12, 64-69 (1997)

14 R. NOWAK and C.L. LI,
Evaluation of HfN Thin Films Considered as Diffusion Barriers In Al/HfN/Si System,
Thin Solid Films, 305, 297-303 (1997)

Acknowledgments

CHUNLIANG LI
January, 2000
Osaka, Japan